Eddy-Mediated Regime Transitions in the Seasonal Cycle of a Hadley Circulation and Implications for Monsoon Dynamics

TAPIO SCHNEIDER

California Institute of Technology, Pasadena, California

SIMONA BORDONI*

Department of Atmospheric and Oceanic Sciences, University of California, Los Angeles, Los Angeles, California

(Manuscript received 2 February 2007, in final form 12 June 2007)

ABSTRACT

In a simulation of seasonal cycles with an idealized general circulation model without a hydrologic cycle and with zonally symmetric boundary conditions, the Hadley cells undergo transitions between two regimes distinguishable according to whether large-scale eddy momentum fluxes strongly or weakly influence the strength of a cell. The center of the summer and equinox Hadley cell lies in a latitude zone of upper-level westerlies and significant eddy momentum flux divergence; the influence of eddy momentum fluxes on the strength of the cell is strong. The center of the cross-equatorial winter Hadley cell lies in a latitude zone of upper-level easterlies and is shielded from the energy-containing midlatitude eddies; the influence of eddy momentum fluxes on the strength of the cell is weak. Mediated by feedbacks between eddy fluxes, mean zonal winds at upper levels, and the mean meridional circulation, the dominant balance in the zonal momentum equation at the center of a Hadley cell shifts at the transitions between the regimes, from eddies dominating the momentum flux divergence in the summer and equinox cell to the mean meridional circulation dominating in the winter cell. At the transitions, a feedback involving changes in the strength of the lower-level temperature advection and in the latitude of the boundary between the winter and summer cell is responsible for changes in the strength of the cross-equatorial winter cell. The transitions resemble the onset and end of monsoons, for example, in the shift in the dominant zonal momentum balance, rapid shifts in the latitudes of maximum meridional mass flux and of maximum convergence at lower levels, rapid changes in strength of the upward mass flux, and changes in direction and strength of the zonal wind at upper and lower levels. In the monsoonal regime, the maximum upward mass flux occurs in an off-equatorial convergence zone located where the balance of the meridional geopotential gradient in the planetary boundary layer shifts from nonlinear frictional to geostrophic. Similar dynamic mechanisms as at the regime transitions in the simulation—mechanisms that can act irrespective of land–sea contrasts and other inhomogeneities in lower boundary conditions—may be implicated in large-scale monsoon dynamics in Earth's atmosphere.

1. Introduction

In Earth's atmosphere, large-scale eddy momentum fluxes strongly influence the strength of the summer Hadley cell but less strongly influence the strength of the cross-equatorial winter Hadley cell. Where frictional processes and the vertical advection of momentum by the mean meridional circulation can be neglected—in the upper branches of the circulation where streamlines are horizontal—the mean zonal momentum balance in a statistically steady state is approximately

$$(f + \bar{\zeta})\bar{v} = f(1 - \mathrm{Ro})\bar{v} \approx \mathcal{S}, \tag{1}$$

with local Rossby number $\mathrm{Ro} = -\bar{\zeta}/f$, eddy momentum flux divergence $\mathcal{S}$, and with the bar denoting a temporal and zonal mean along isobars (other symbols have their usual meaning). The zonal momentum balance (1) typically holds in the upper branch near the center of a Hadley cell. It relates the strength of the Hadley cell (a vertical integral of the meridional mass flux at the center of the cell) to the Coriolis parameter, the local

* Current affiliation: California Institute of Technology, Pasadena, California.

Corresponding author address: Tapio Schneider, California Institute of Technology, Pasadena, CA 91125-2300.
E-mail: tapio@caltech.edu

DOI: 10.1175/2007JAS2415.1

Rossby number, and the eddy momentum flux divergence. The local Rossby number in the upper branch of a Hadley cell, where streamlines are horizontal, is a nondimensional measure of the influence of eddy momentum fluxes on the strength of the cell, or, because the absolute vorticity $f + \bar{\zeta} = f(1 - \mathrm{Ro}) = -(a^2 \cos\phi)^{-1}\partial_\phi \overline{m}$ is proportional to the meridional gradient of absolute angular momentum per unit mass $\overline{m} = (\Omega a \cos\phi + \overline{u})a \cos\phi$, it is a nondimensional measure of the flatness of angular momentum contours in the meridional plane (e.g., Schneider 2006). If $\mathrm{Ro} \to 0$, angular momentum contours are vertical; the mean meridional circulation is tied to the eddy momentum flux divergence. If $\mathrm{Ro} \to 1$, angular momentum contours are horizontal; the eddy momentum flux divergence approaches zero, and the mean meridional circulation decouples from the eddy momentum flux divergence. The local Rossby number in the upper branches of Earth's Hadley cells varies from $\mathrm{Ro} \lesssim 0.2$ in the summer cell to $\mathrm{Ro} \gtrsim 0.5$ in the cross-equatorial winter cell, with intermediate values in the equinox cells (Walker and Schneider 2006). Regionally, in the Asian summer monsoon anticyclone, local Rossby numbers can reach about 0.7 according to monthly-mean reanalysis data (Uppala et al. 2005).

Depending on whether eddy momentum fluxes strongly or weakly influence its strength, a Hadley cell responds differently to variations in thermal driving. The strength of a Hadley cell with $\mathrm{Ro} \to 0$ in the upper branch does not respond directly to variations in thermal driving. According to the zonal momentum balance (1), it responds only indirectly through changes in eddy momentum flux divergence and, possibly, through changes in the Hadley cell extent, which affect the relevant value of the Coriolis parameter at the center of the cell (Walker and Schneider 2006). The strength of a Hadley cell with $\mathrm{Ro} \to 1$ in the upper branch—a Hadley cell in the angular momentum–conserving limit in which streamlines and angular momentum contours coincide—responds directly to variations in thermal driving (Schneider 1977; Held and Hou 1980; Lindzen and Hou 1988). The seasonal variations of the local Rossby number in the upper branches of Earth's Hadley cells lie between these extremes and suggest that the character of a Hadley cell's response to variations in thermal driving may change in the course of a seasonal cycle.

Using simulations with an idealized general circulation model (GCM) with zonally symmetric boundary conditions, Walker and Schneider (2006) showed that, depending on the latitude of maximum radiative-equilibrium temperature, statistically steady Hadley cells are in one of two regimes distinguishable according to whether eddy momentum fluxes strongly or weakly influence the strength of the cells. Here we use a slightly modified version of Walker and Schneider's GCM to simulate not only statistically steady states but also seasonal cycles of a Hadley circulation. We show that in the course of a simulated seasonal cycle, Hadley cells undergo transitions between the two regimes, and we analyze the dynamic mechanisms involved in the transitions. We argue that similar dynamic mechanisms may be implicated in large-scale monsoon dynamics in Earth's atmosphere.

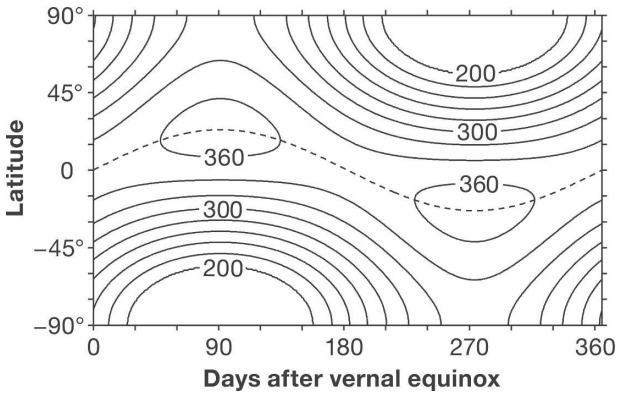

FIG. 1. Seasonal cycle of radiative-equilibrium surface temperature (solid contours, contour interval 20 K) and latitude ϕ_0 of its maximum (dashed line).

2. Idealized GCM

Radiative heating and cooling in the idealized GCM are represented by Newtonian relaxation of temperatures toward a radiative-equilibrium state of a semigray atmosphere, which is axisymmetric and statically unstable in the lower troposphere. The surface temperature in radiative equilibrium as a function of latitude ϕ is prescribed as

$$T_s^e = \max\left\{\check{T}_s^e, \hat{T}_s^e - \Delta_h[\sin^2\phi - 2\sin\phi_0(t)\sin\phi]\right\}, \quad (2)$$

with minimum temperature $\check{T}_s^e = 200$ K, equatorial temperature $\hat{T}_s^e = 350$ K, and equinoctial pole–equator temperature contrast $\Delta_h = 112.5$ K. In the simulations of statistically steady states, the latitude ϕ_0 of maximum radiative-equilibrium temperature is a fixed parameter; in the simulation of seasonal cycles, it varies with time t according to

$$\phi_0(t) = 23.5° \sin(2\pi t/365\ \mathrm{d}), \quad (3)$$

with $t = 0$ corresponding to vernal equinox. Figure 1 shows the resulting seasonal cycle of radiative-equilibrium surface temperature. The radiative-equilibrium

temperature decreases with altitude to a constant temperature of 200 K at the top of the atmosphere, in the same way as in the simulations of Schneider (2004) and Schneider and Walker (2006). The truncation of the radiative-equilibrium surface temperature at $\check{T}_s^e = 200$ K, which may be viewed as representing a polar-night effect, ensures that the radiative-equilibrium surface temperature in high latitudes of the winter hemisphere does not become smaller than the radiative-equilibrium temperature at the top of the atmosphere.

The Newtonian relaxation time is 50 days in the interior atmosphere (at sigma levels above $\sigma = 0.85$) and increases at the surface from a minimum value of 7 days at the latitude ϕ_0 to 50 days far away from it. The latitude dependence of the relaxation coefficient (inverse relaxation time) at the surface is Gaussian, with standard deviation 20°. The transition in the relaxation coefficient between the surface and the interior atmosphere is linear in the model's vertical sigma coordinate, as in the simulations of Held and Suarez (1994), Schneider (2004), and Schneider and Walker (2006). Although the resulting Newtonian temperature relaxation rate is not easily justifiable as a radiative heating rate, we will call it, for simplicity, a radiative heating rate.

The radiative-heating formulation is chosen such that the dynamic mechanisms under investigation here are exposed clearly in a statistically axisymmetric simulated climate in which features such as the dominant balance in the zonal momentum equation mimic the local climate and its seasonal variations in Earth's large-scale monsoon regions. For example, to compensate for a lack of thermal inertia of the model surface, the radiative-equilibrium surface temperature maximum (3) exhibits smaller seasonal excursions away from the equator than Earth's insolation maximum. Increasing the Newtonian relaxation coefficient near the surface near latitude ϕ_0 and so making it time dependent in the seasonal-cycle simulation likewise is an empiricism, as in the simulations of Held and Suarez (1994) and Schneider (2004), to obtain a simulated climate resembling Earth's. We have conducted a simulation with constant Newtonian relaxation rate (25 days) throughout the atmosphere, with results qualitatively similar to those discussed in this paper; however, the lower branches of the solstitial Hadley cells in that simulation occupy half the troposphere (cf. Walker and Schneider 2006, their Fig. 15), unlike in Earth's atmosphere and in the simulations discussed in this paper, in which they are confined near the surface. It is crucial for the dynamic mechanisms under investigation here that the near-surface temperature can adjust dynamically and is not as strongly constrained as it is, for example, in simulations with a prescribed surface temperature.

In all respects other than the radiative-heating formulation, the idealized GCM is the same as that described by Schneider and Walker (2006) and used by Walker and Schneider (2006). The spherical model surface is spatially uniform and thermally insulating. Turbulent mixing in a planetary boundary layer of fixed height (2.5 km) is represented as vertical diffusion of momentum and dry static energy, with turbulent Prandtl number one (Smagorinsky et al. 1965). The model does not include a hydrologic cycle. However, a convection scheme mimics the stabilizing effect of latent heat release in moist convection by relaxing temperatures in an atmospheric column to an enthalpy–conserving profile with lapse rate $0.7\Gamma_d = 6.8$ K km^{-1}, with dry-adiabatic lapse rate Γ_d, whenever an atmospheric column is less stable than a column with temperature lapse rate $0.7\Gamma_d$. Although this ignores dynamically important effects of an active hydrologic cycle, it results in simulated atmospheric circulations that resemble Earth's mean circulation in several respects, such as temperature lapse rates and structures of zonal jets (Schneider and Walker 2006; Walker and Schneider 2006).

The model was run at spectral resolution T42 with 30 sigma-coordinate levels in the vertical. We conducted simulations with fixed latitudes $0° \leq \phi_0 \leq 23.5°$ of maximum radiative-equilibrium temperature to obtain statistically steady states. Section 3 gives a brief overview of results from these simulations (averages over 100 simulated days). The simulation of seasonal cycles was started from an equinox ($\phi_0 = 0°$) statistically steady state and was run for 20 simulated years. Sections 4–6 discuss results from this simulation (averages over the last 17 years of the simulation).

3. Statistically steady states

Figure 2 shows the strength of the cross-equatorial Hadley cell in steady-state simulations with different values of the latitude ϕ_0 of maximum radiative-equilibrium temperature. The scaling of the cross-equatorial Hadley cell strength as a function of ϕ_0 is in two regimes: for $\phi_0 \lesssim 9°$, the strength increases weakly with ϕ_0 (roughly as $\phi_0^{1/5}$); for $\phi_0 \gtrsim 9°$, the strength increases more strongly with ϕ_0 (roughly as $\phi_0^{3/4}$). A similar transition in scaling regimes occurred in the simulations of Walker and Schneider (2006), but quantitative details differ because the radiative-heating formulations differ.

Figure 3 shows the streamfunction of the mean meridional circulation, the angular momentum, the hori-

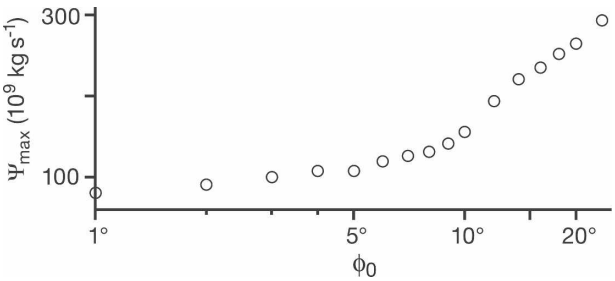

FIG. 2. Strength Ψ_{max} of cross-equatorial Hadley cell as function of ϕ_0 in simulations of statistically steady states. The strength is the maximum value of the streamfunction of the mean meridional circulation above the level $\sigma = 0.85$. The scale of the ϕ_0 axis is logarithmic.

zontal eddy momentum flux divergence, and the zonal wind for four values of ϕ_0. Mean fields are surface pressure-weighted sigma-coordinate averages over longitude and time; eddy fields are deviations from these mean fields. Only the horizontal eddy momentum flux divergence is shown in the figure. The vertical eddy momentum flux divergence is generally small compared with the horizontal eddy momentum flux divergence, except in zones of large vertical shear at the subtropical boundaries of the Hadley cells, particularly of the strong cross-equatorial cells.

It can be seen that, as in the simulations of Walker and Schneider (2006), the transition in scaling regimes recognizable in Fig. 2 occurs when the streamfunction maximum of the cross-equatorial (southern) Hadley cell moves across the equator. For $\phi_0 \lesssim 9°$, the streamfunction maximum is in the Southern Hemisphere; for $\phi_0 \gtrsim 9°$, the streamfunction maximum is near the equator in the Northern Hemisphere.

As the streamfunction maximum of the southern Hadley cell moves across the equator, it moves from a latitude zone of upper-level westerlies and significant eddy momentum flux divergence into a latitude zone of upper-level easterlies and weak eddy momentum flux divergence. Significant eddy momentum flux diver-

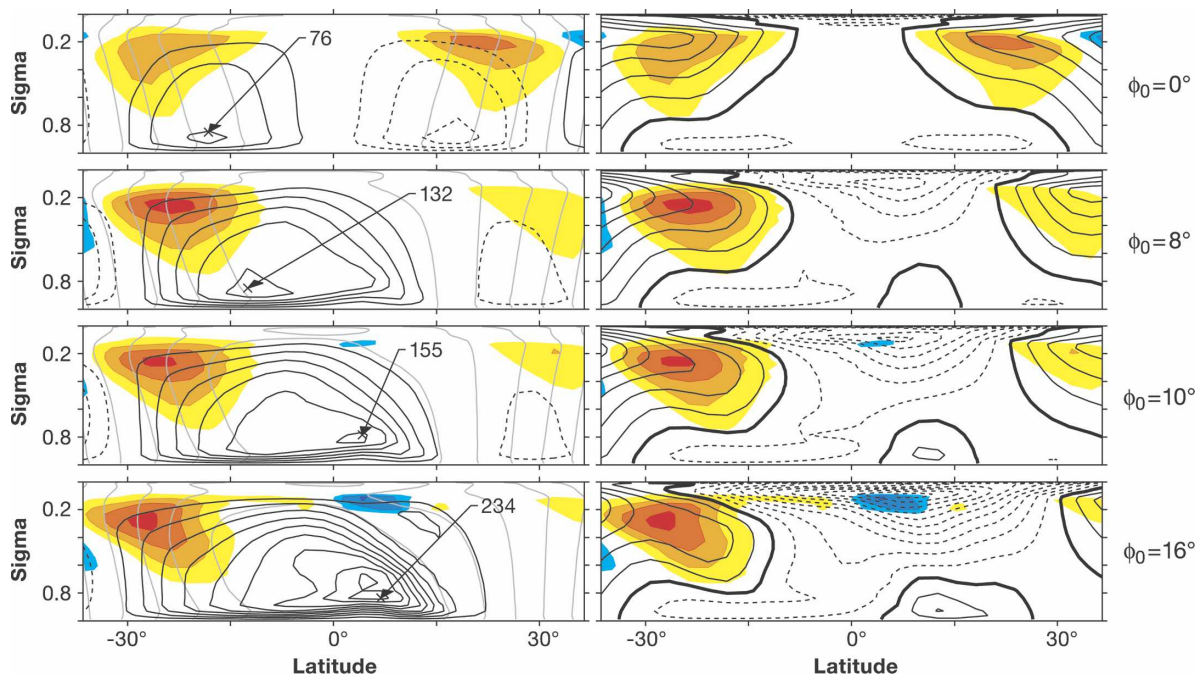

FIG. 3. Mean circulations in statistically steady states. Rows correspond to latitudes ϕ_0 of maximum radiative-equilibrium temperature indicated on the right. In the left column, black contours indicate streamfunction of mean meridional circulation (contour interval 25×10^9 kg s^{-1}), with solid contours for positive values (counterclockwise rotation) and dashed contours for negative values (clockwise rotation). Gray contours indicate mean absolute angular momentum per unit mass (contour interval $\Omega a^2/15$). Colors indicate horizontal eddy momentum flux divergence, div $(\overline{p}_s \overline{u'v'}^{\sigma} \cos\phi)/\overline{p}_s$, with $\overline{p}_s$ denoting the temporal and zonal mean surface pressure, $\overline{(\cdot)}^{\sigma}$ denoting a surface pressure–weighted temporal and zonal mean along sigma surfaces, and primes denoting deviations from this mean (contour interval 8×10^{-6} m s^{-2}, with red tones for positive and blue tones for negative values). Arrows identify streamfunction maxima above $\sigma = 0.85$ (maximum values given in units of 10^9 kg s^{-1}). In the right column, black contours indicate mean zonal wind (contour interval 6 m s^{-1}, negative contours dashed and zero contour thick); colors indicate horizontal eddy momentum flux divergence as in the left column. For $\phi_0 = 0°$, the two hemispheres are statistically identical; the deviations from hemispheric symmetry seen in the figure are indicative of the sampling variability in the averages.

gence is generally confined to regions of westerlies, whereas regions of easterlies are shielded from the energy-containing midlatitude eddies so that the eddy momentum flux divergence there is weak (Charney 1969; Webster and Holton 1982). For $\phi_0 = 0°$, upper-level westerlies and significant eddy momentum flux divergence extend to the latitudes of the centers of the Hadley cells, and streamlines cross angular momentum contours in the upper branches of the cells, indicating that eddy momentum fluxes influence their strength. The local Rossby number in the upper branches of the Hadley cells, near the latitudes of the streamfunction extrema, is relatively small, increasing with altitude from 0.2 to 0.4. As ϕ_0 increases, the local Rossby number in the upper branch of the southern Hadley cell increases, and that in the upper branch of the northern Hadley cell decreases. For $\phi_0 = 8°$, the local Rossby number in the upper branches, near the streamfunction extrema, increases with altitude from 0.3 to 0.7 in the southern cell and from 0.1 to 0.3 in the northern cell. For $\phi_0 \gtrsim 9°$, when the streamfunction maximum of the southern Hadley cell is near the equator or in the Northern Hemisphere in a latitude zone of upper-level easterlies and weak eddy momentum flux divergence, the ascending branch of the southern Hadley cell is close to angular momentum conserving, though local Rossby numbers above the streamfunction maximum are no longer meaningful because streamlines are not horizontal there but approximately follow slanted angular momentum contours. The northern Hadley cell for $\phi_0 \gtrsim 9°$ is controlled by eddy momentum fluxes, with $\mathrm{Ro} \lesssim 0.3$ in the upper branch. At the transition in scaling regimes of the cross-equatorial Hadley cell, then, the influence of eddy momentum fluxes on the strength of the cell shifts from strong for $\phi_0 \lesssim 9°$ to weak for $\phi_0 \gtrsim 9°$.

From the zonal momentum balance above the planetary boundary layer in a statistically steady state,

$$f\bar{v} = \mathcal{S} + \mathcal{M}, \tag{4}$$

with momentum flux divergences $\mathcal{S}$ and $\mathcal{M}$ associated with eddies and with the mean meridional circulation, it follows that the streamfunction Ψ of the mean meridional circulation above the boundary layer can be decomposed into a component

$$\Psi_e(\phi, p) = -\frac{2\pi a \cos\phi}{fg} \int_0^p \mathcal{S}\, dp',$$

associated with eddy momentum fluxes, and a component

$$\Psi_m(\phi, p) = -\frac{2\pi a \cos\phi}{fg} \int_0^p \mathcal{M}\, dp',$$

associated with mean momentum fluxes.[1] Figure 4 shows the streamfunction components Ψ_e and Ψ_m for the same four values of ϕ_0 as in Fig. 3. Both Ψ_e and Ψ_m include contributions from vertical momentum flux divergences, but these are generally small compared with the contributions from horizontal momentum flux divergences. Above the boundary layer, the sum of the streamfunction components $\Psi_e + \Psi_m$ is equal to the streamfunction Ψ of the mean meridional circulation (up to a small residual owing to time dependence of the finite-time average); in the boundary layer, the streamfunction Ψ has an additional component associated with the mean turbulent drag on the zonal wind. Figure 4 shows that, for $\phi_0 \lesssim 9°$, the streamfunction component Ψ_e dominates globally, with a maximum in the Southern Hemisphere. For $\phi_0 \gtrsim 9°$, the streamfunction component Ψ_e remains dominant locally in the Southern Hemisphere, in the descending branch of the cross-equatorial Hadley cell, but the streamfunction component Ψ_m dominates globally, with a maximum in the Northern Hemisphere. This demonstrates explicitly that, as indicated by the local Rossby numbers, the transition in scaling regimes marks a shift in the dominant balance in the zonal momentum equation (4) near the center of the cross-equatorial Hadley cell, from eddy fluxes dominating the momentum flux divergence for $\phi_0 \lesssim 9°$ to the mean meridional circulation dominating for $\phi_0 \gtrsim 9°$.

This brief overview of the statistically steady states serves as a reference point for our discussion of the seasonal cycle, which will also elucidate aspects of the statistically steady states.

4. Seasonal cycle

Figure 5 shows the same quantities as Fig. 3, but now for four pentads in the course of the simulated seasonal cycle. Mean fields are now averages over longitude and over the corresponding pentad of the simulated years, and eddy fields are deviations from these mean fields. The streamfunction of the mean meridional circulation is proportional to the vertical integral from the surface upward of the meridional mass flux averaged along sigma surfaces; that is, time dependence of the surface pressure averaged over a pentad is ignored in the cal-

[1] For simplicity, we use pressure coordinates in theoretical developments in this paper. The simulation results shown are based on averages in the GCM's sigma coordinates, for which means along isobars must be replaced by surface pressure–weighted means along sigma surfaces, with a corresponding definition of eddy fields as deviations from these means and a weighting in flux divergences by the mean surface pressure.

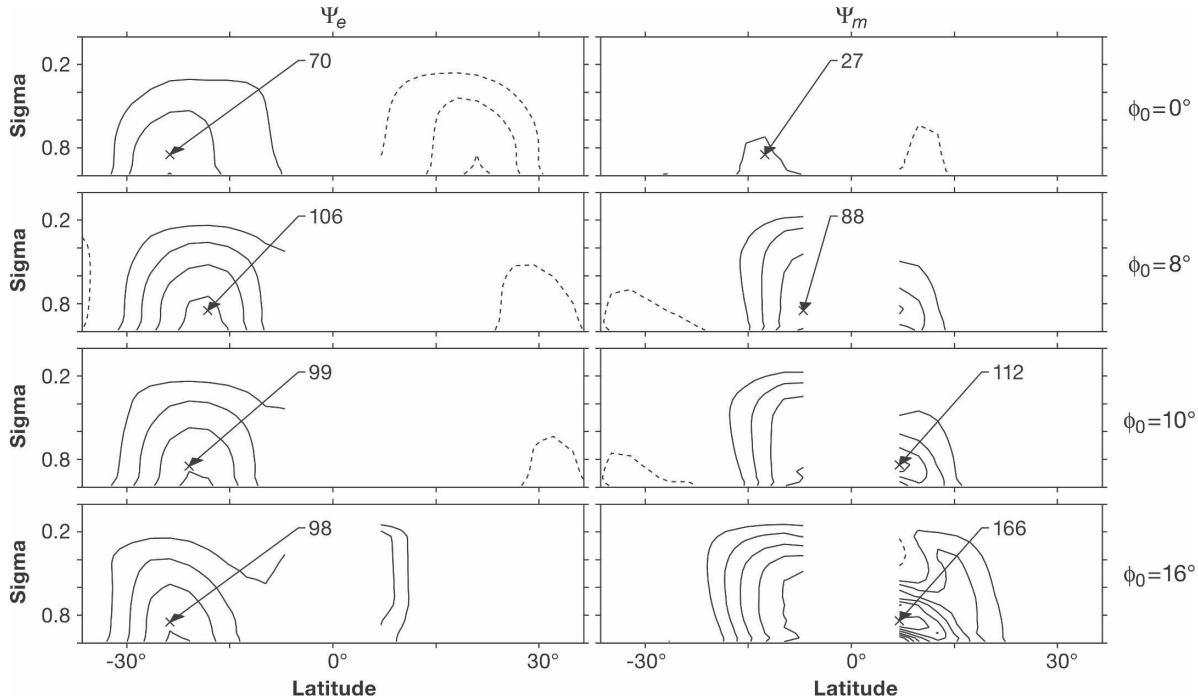

FIG. 4. Streamfunction components associated with (left) eddy momentum flux divergence and (right) mean momentum flux divergence. Rows correspond to the same four latitudes ϕ_0 of maximum radiative-equilibrium temperature as in Fig. 3. The streamfunction components are calculated as $\Psi_e = -2\pi a/(fg) \int_0^\sigma \mathrm{div}\,[\overline{p}_s \cos\phi(\overline{u'v'}^\sigma, \overline{u'\dot{\sigma}'}^\sigma)]\, d\sigma'$ and $\Psi_m = -2\pi a/(fg) \int_0^\sigma \mathrm{div}\,[\overline{p}_s \cos\phi(\overline{u}^\sigma \overline{v}^\sigma, \overline{u}^\sigma \overline{\dot{\sigma}}^\sigma)]\, d\sigma'$, where $\dot{\sigma} = D\sigma/Dt$. Streamfunction components within 4.2° of the equator, where they are poorly defined because the Coriolis parameter approaches zero, are not shown. Arrows identify streamfunction maxima above $\sigma = 0.85$ (maximum values given in units of 10^9 kg s^{-1}).

culation of the streamfunction. Ignoring surface pressure tendencies is justified by the fact that the streamlines shown in Fig. 5 close (absolute values of the streamfunction at the top of the atmosphere do not exceed 7% of the maximum absolute value in any pentad).

The same regime transition identified in the steady-state simulations occurs in the seasonal-cycle simulation. At day 1–5 (first row of Fig. 5), immediately after vernal equinox, streamlines of the mean meridional circulation cross angular momentum contours throughout both Hadley cells, indicating that eddy momentum fluxes significantly influence the cells. The local Rossby number in the upper branches, near the latitudes of the streamfunction extrema, increases with altitude from 0.2 to 0.5 in the southern cell and from 0.3 to 0.5 in the northern cell—comparable with local Rossby numbers in Earth's equinox Hadley cells. The asymmetry between the hemispheres indicates a delayed response of the circulation to variations in thermal driving. The eddy momentum flux divergence and, associated with it, the Hadley cell are stronger in the Northern Hemisphere, which is emerging from winter and exhibits an equator–pole surface potential temperature contrast twice as large as that of the Southern Hemisphere (approximately 53 versus 26 K).

By day 26–30 (second row), the southern Hadley cell has strengthened and the northern Hadley cell has weakened. Eddy momentum fluxes influence both cells. The local Rossby number in the upper branches increases with altitude from 0.1 to 0.5 in the southern cell and from 0.2 to 0.4 in the northern cell. The southern cell has acquired a weak cross-equatorial component. In the boundary layer, if one neglects horizontal eddy momentum fluxes and the vertical advection of momentum by the mean meridional circulation, the zonal momentum balance is approximately

$$(f + \overline{\zeta})\overline{v} = f(1 - \mathrm{Ro})\overline{v} \approx -\mathcal{D}, \tag{5}$$

with mean turbulent drag $\mathcal{D}$ on the zonal wind. Ekman balance corresponds to $\mathrm{Ro} \to 0$ in the boundary layer and, at day 26–30, is a good approximation, with $|\mathrm{Ro}| \lesssim 0.25$, outside 4° of the equator. Within 2° of the equator in the Northern Hemisphere, the local Rossby number in the boundary layer exceeds one, corresponding to $f\,(f + \overline{\zeta}) < 0$, as in the observations and simulations of Krishnamurti et al. (1981), Yang and Krishnamurti (1981), and Tomas et al. (1999). So, consistent

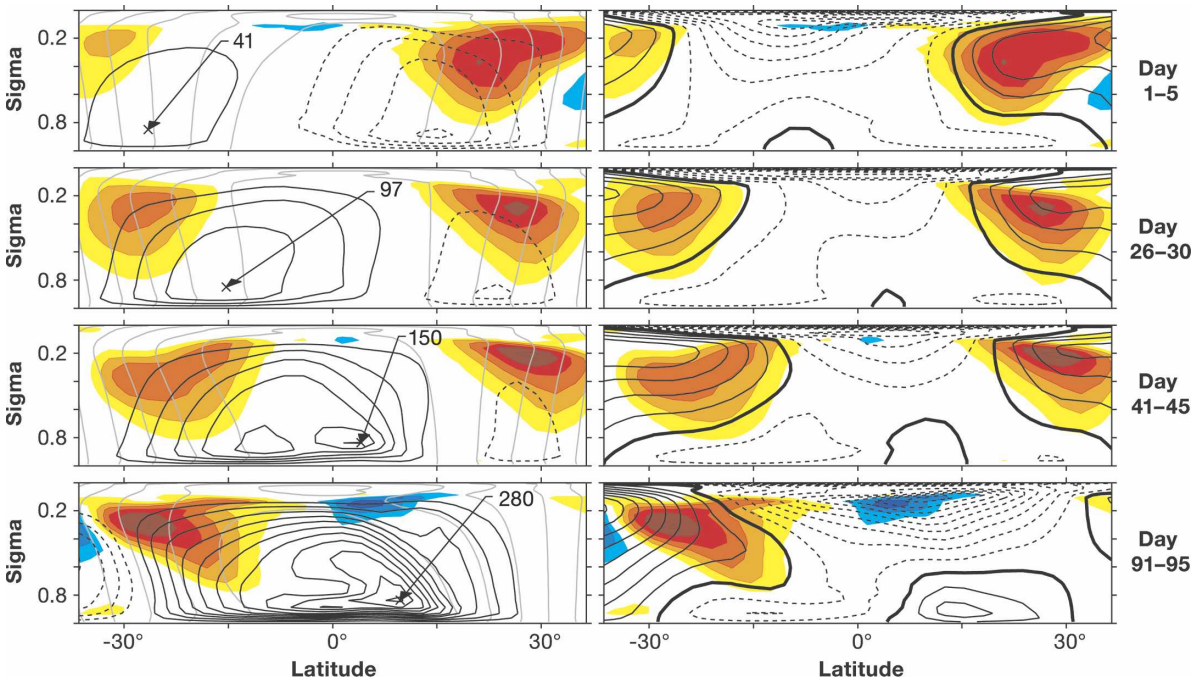

FIG. 5. Mean circulations at four pentads in the course of the seasonal cycle. Rows correspond to the pentads indicated on the right (in days after vernal equinox). Quantities shown and contour intervals are as in Fig. 3 except that the contour interval of the horizontal eddy momentum flux divergence is 4×10^{-6} m s^{-2} in the top three rows and 8×10^{-6} m s^{-2} in the bottom row.

with the zonal momentum balance (5) with Ro < 1 outside a few degrees of the equator and with the weak northward flow across the equator, weak lower-level westerlies have appeared north of the equator. The streamfunction maximum of the southern Hadley cell has moved equatorward, as it did for increasing $\phi_0 \lesssim 9°$ in the steady-state simulations (cf. Fig. 3); however, it remains in the Southern Hemisphere, near the latitude at which the upper-level zonal wind changes sign and the eddy momentum flux divergence becomes small.

By day 41–45 (third row), the southern Hadley cell is undergoing a transition. Over a 15-day period, its streamfunction maximum has moved from $-15°$ in the Southern Hemisphere to 4° in the Northern Hemisphere, and the maximum streamfunction value has increased by 55%. The streamfunction maximum has moved into a latitude zone of upper-level easterlies, where it is shielded from the energy-containing midlatitude eddies and where the eddy momentum flux divergence is small. Consistent with the zonal momentum balance (5) and with the strengthened northward flow across the equator, the lower-level westerlies north of the equator, in the latitude zone of the cross-equatorial Hadley cell, have likewise strengthened. (At day 41–45, Ekman balance is a good approximation in the boundary layer, with $|\mathrm{Ro}| < 0.25$, outside 8° of the equator, and Ro > 1 within 2°–5° of the equator in the Northern Hemisphere.) The ascending branch of the cross-equatorial Hadley cell now is close to angular momentum conserving: streamlines approximately follow slanted angular momentum surfaces. The cross-equatorial Hadley cell has displaced angular momentum contours from the vertical, but streamlines still cross angular momentum contours in the descending branch, in the region of upper-level westerlies and significant eddy momentum flux divergence in the Southern Hemisphere, where a secondary streamfunction maximum remains (see also the steady-state streamfunction and its components in Figs. 3 and 4). The weak northern Hadley cell now is controlled by eddy momentum flux divergence, with Ro $\lesssim 0.1$ in its upper branch.

As the latitude ϕ_0 of maximum radiative-equilibrium temperature moves farther into the Northern Hemisphere, the southern Hadley cell continues to strengthen, with a streamfunction maximum in the Northern Hemisphere that does not move beyond 10° latitude. By day 91–95 (fourth row), at northern solstice, the southern (winter) Hadley cell extends to about 31° latitude into the Northern (summer) Hemisphere. This is approximately the latitude of maximum vertically averaged temperature or—because the temperature lapse rate near the center and in the ascending branch of the Hadley cell is approximately the convective lapse rate—the latitude of maximum lower-level

temperature or potential temperature (Privé and Plumb 2007a,b; see also Figs. 8 and 11 below). However, the streamfunction maximum is at 9° latitude, and the maximum upward mass flux at lower levels occurs near 15° latitude. Consistent with the zonal momentum balance (5) and with the further strengthened northward flow across the equator, off-equatorial lower-level westerlies in the summer hemisphere and easterlies in the winter hemisphere have likewise strengthened. (At day 91–95, Ekman balance is a good approximation in the boundary layer, with $|\mathrm{Ro}| < 0.25$, outside 13° of the equator, and $\mathrm{Ro} > 1$ within about 2°–8° of the equator in the summer hemisphere.) The zonal wind in the upper troposphere throughout the tropics is now easterly and strong, shielding most of the winter Hadley cell, except its descending branch, from the energy-containing midlatitude eddies. The ascending branch of the winter Hadley cell is nearly angular momentum conserving, as is apparent from the near coincidence of streamlines and angular momentum contours there. However, as in the steady-state simulations for $\phi_0 \gtrsim 9°$ (Fig. 3), there is weak eddy momentum flux convergence in a thin layer in the upper troposphere at and equatorward of the latitude of maximum upward mass flux, indicating propagation of wave activity out of this region. The meridional gradient of potential vorticity along isentropes is reversed (negative) near the center of this region, suggesting that the momentum flux convergence is associated with eddies generated by barotropic instability [see Hsu and Plumb (2000) and Plumb (2007) for a discussion of a similar but zonally localized instability]. The summer Hadley cell is very weak (streamfunction maximum about 15×10^9 kg s^{-1}) and is controlled by eddy momentum flux divergence ($\mathrm{Ro} \lesssim 0.1$).

A similar but reverse succession of circulation changes occurs between northern solstice and autumnal equinox, as the latitude ϕ_0 of maximum radiative-equilibrium temperature moves back toward the equator. As ϕ_0 moves farther southward from autumnal equinox through southern solstice, by statistical symmetry of the two hemispheres, changes occur that are symmetric to those seen as ϕ_0 moves northward from vernal equinox through northern solstice.

Figure 6 shows the time evolution of circulation statistics over the seasonal cycle. Many circulation features occurring in the course of the seasonal cycle resemble circulation features in the steady-state simulations, but they occur with a delay caused by thermal and dynamic inertia. For example, the cross-equatorial streamfunction extremum moves across the equator at $|\phi_0| \approx 9°$ in the steady-state simulations (Fig. 3), corresponding to about 23 days after equinox, whereas it moves across the equator about 40 days after equinox in the seasonal-cycle simulation (Figs. 5 and 6b). Statistically steady states in a perpetual equinox simulation exhibit weak upper-level easterlies near the equator (Fig. 3), whereas the weakest upper-level easterlies in the seasonal-cycle simulation occur about a month after the equinoxes (Fig. 6c). Similar delays in the atmospheric response to seasonal variations in thermal driving are seen in the simulations with a comprehensive GCM by Mapes et al. (2005).

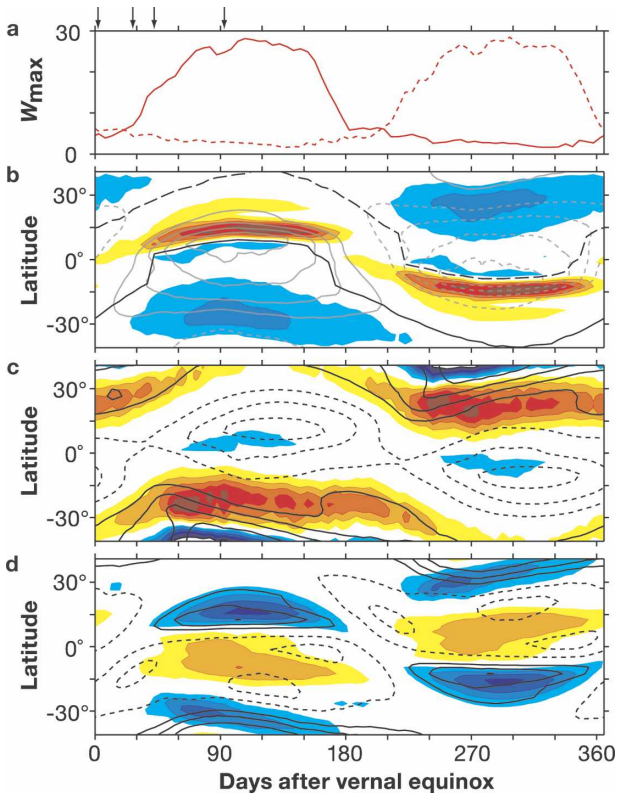

FIG. 6. Seasonal cycle of circulation statistics. (a) Maximum value of lower-level upward mass flux $W = -\mu\bar{\dot{\sigma}}^{\sigma}$ (10^4 kg m^{-1} s^{-1}) in the southern Hadley cell (solid) and northern Hadley cell (dashed), where $\mu = 2\pi a \cos\phi \times \bar{p}_s/g$ is the atmospheric mass per unit length in a meridional cross section. (b) Lower-level upward mass flux W (colors, contour interval 5×10^4 kg m^{-1} s^{-1}), lower-level streamfunction of mean meridional circulation (gray contours, contour interval 60×10^9 kg s^{-1}), and position of the lower-level streamfunction maximum and minimum (solid and dashed black lines). (c) Vertically integrated eddy momentum flux divergence $2\pi a/g \int \mathrm{div}\,(\bar{p}_s\,\overline{u'v'}^{\sigma} \cos\phi)\, d\sigma$ (colors, contour interval 1.25×10^6 kg s^{-2}) and mean upper-level zonal wind (black contours, contour interval 10 m s^{-1}). (d) Vertically integrated mean momentum flux divergence $2\pi a/g \int \mathrm{div}\,(\bar{p}_s\,\bar{u}^{\sigma}\bar{v}^{\sigma} \cos\phi)\, d\sigma$ (colors, contour interval 1.25×10^6 kg s^{-2}) and mean lower-level zonal wind (black contours, contour interval 4 m s^{-1}). Lower-level quantities are evaluated at $\sigma = 0.85$, upper-level quantities at $\sigma = 0.3$. Red tones and solid contours indicate positive values; blue tones and dashed contours negative values. Zero contours are not shown. Arrows at the top indicate times at which meridional cross sections are shown in Fig. 5.

At the transition of a Hadley cell from the summer and equinox regime, in which eddy momentum flux influences are strong, into the winter regime, in which eddy momentum flux influences are weak, the streamfunction extremum shifts rapidly compared with the time scale of variations in ϕ_0 from the winter into the summer hemisphere. Figure 6b shows this shift for the streamfunction extremum at the fixed lower level $\sigma = 0.85$, which in our simulation is generally, as in Fig. 5, close to the level of the overall streamfunction extremum. Because the streamfunction at a given level is the vertical integral of the mean meridional mass flux from the surface to that level, the mean vertical mass flux, by continuity, approximately vanishes at the latitude of the streamfunction extremum at a given level (time dependence of the surface pressure is negligible in the continuity relation of lower-level mean meridional and vertical mass fluxes). So the inner boundary of the region of lower-level upward mass flux in the Hadley cell likewise shifts rapidly into the summer hemisphere (Fig. 6b). The strength of the lower-level upward mass flux increases, with maximum values increasing from values around 2 to 5×10^4 kg m^{-1} s^{-1} in the summer and equinox regime to values around 27×10^4 kg m^{-1} s^{-1} in the winter regime of a Hadley cell (Fig. 6a). In the winter regime, the latitude of maximum upward mass flux at lower levels remains between 10° and 15° in the summer hemisphere, as in the steady-state simulations (Fig. 3). A secondary maximum forms poleward of the primary maximum, just equatorward of the lower-level potential temperature maximum and of the boundary between the cross-equatorial winter Hadley cell and the summer Hadley cell. This secondary maximum moves farther into the summer hemisphere as $|\phi_0|$ increases (Fig. 6b). A reverse, albeit not entirely symmetric, transition of the cross-equatorial Hadley cell from the winter regime into the equinox and summer regime occurs just before the subsequent equinox (Fig. 6).

That the transitions of a Hadley cell between the summer and equinox regime and the winter regime mark a shift in the dominant zonal momentum balance, as in the steady-state simulations, can also be seen from the vertically integrated momentum flux divergences associated with eddies and with the mean meridional circulation. In the summer and equinox regime, the eddy momentum flux divergence dominates near the latitude of the streamfunction extremum. In the winter regime, the mean momentum flux divergence dominates within the Hadley cell except near its boundary in the winter subtropics (cf. Figs. 6c and 6d). The cross-equatorial Hadley cell in the winter regime transports momentum from the region of lower-level easterlies in low latitudes of the winter hemisphere into the winter subtropics (Fig. 6d), from where eddies transport it farther poleward (Figs. 6c). It also transports momentum into the region of lower-level westerlies in low latitudes of the summer hemisphere (Fig. 6d), where the dominant balance in the vertically integrated zonal momentum equation is between the convergence of mean momentum flux and the drag on the lower-level westerlies.[2]

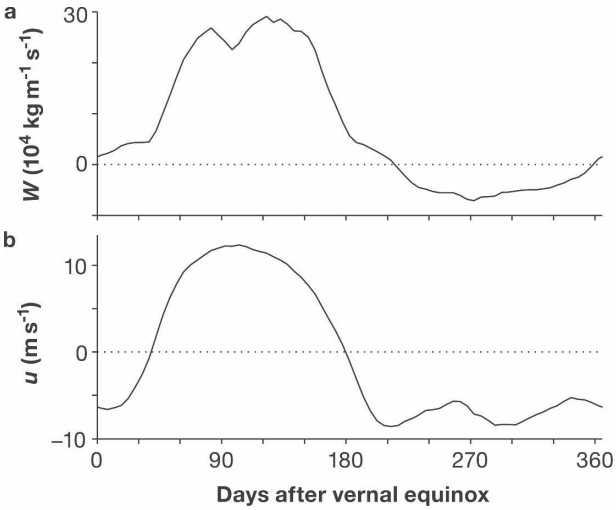

FIG. 7. Seasonal cycle of lower-level mean fields at 13° latitude. (a) Upward mass flux W and (b) zonal wind. Both quantities are evaluated at $\sigma = 0.85$.

The lower-level upward mass flux and zonal wind also vary intraseasonally between the regime transitions (Figs. 6a,b,d). These intraseasonal variations have a component that is coherent with the seasonal cycle in both, statistically identical but independent, hemispheres; therefore, the coherence is unlikely to be an artifact of sampling variability. Intraseasonal variability that is similarly phase locked to the seasonal cycle occurs in monsoon regions in Earth's atmosphere (e.g., Lau and Yang 1996).

The rapid shifts in the latitude of the streamfunction extremum at the transitions of a Hadley cell between the summer and equinox regime and the winter regime are associated with rapid local circulation changes. Figure 7 shows two local circulation statistics exhibiting such rapid changes. Shown are the mean upward mass flux and zonal wind at 13° latitude and at $\sigma = 0.85$—that is, sections through Figs. 6b and 6d at fixed latitude—with the latitude chosen as roughly the latitude at which these quantities are maximal in the winter

[2] Time dependence of the vertically integrated zonal wind only plays a moderately significant role in the zonal momentum balance near the transition from the equinox into the winter regime. It is less significant near the reverse transition.

regime of the southern Hadley cell. The local upward mass flux and zonal wind at the transitions between the regimes change on time scales of about 30 days. Compared with the changes at the transitions, the intraseasonal variations of these quantities between the transitions are small.

5. Dynamics of regime transitions

A feedback between nonlinear mean-flow processes leads to the changes in strength of a Hadley cell at the regime transitions, and an eddy–mean flow feedback mediates the transitions and the rapid shifts in the latitude of the streamfunction extremum. Considerations of an idealized axisymmetric Hadley cell in which angular momentum is conserved along streamlines in the free troposphere illuminate these feedbacks and aspects of the circulation in the winter regime.

Angular momentum conservation along a streamline ascending at latitude ϕ_1 from a lower level with negligible zonal wind implies a zonal wind

$$u_m(\phi) = \Omega a \frac{\cos^2\phi_1 - \cos^2\phi}{\cos\phi} \tag{6}$$

at latitude ϕ along the streamline and thus implies easterlies between latitudes ϕ_1 and $-\phi_1$ (Lindzen and Hou 1988). The zonal wind in the free troposphere is approximately in gradient balance with a meridional geopotential gradient along isobars whose baroclinic component, by hydrostatic balance, is associated with a meridional potential temperature gradient. Consider a Hadley cell with ascending branch concentrated near latitude ϕ_1 and upper branch concentrated near an upper-level isobar. If the temperature lapse rate above some lower-level isobar does not depend on latitude and if the meridional geopotential gradient at the lower-level isobar is negligible (consistent with negligible lower-level zonal wind), the geopotential gradient balancing the upper-level angular momentum–conserving wind (6) is associated with the potential temperature

$$\theta_m(\phi) = \theta_{\max} - \theta_0 \frac{\Omega^2 a^2}{2gH} \frac{(\sin^2\phi - \sin^2\phi_1)^2}{\cos^2\phi} \tag{7}$$

at the lower-level isobar, where H is the log-pressure height difference between the lower level and the upper branch of the Hadley cell and θ_0 is a reference potential temperature.[3] This lower-level potential temperature distribution is symmetric about the equator and has maxima $\theta_{\max}$ at $\pm\phi_1$ and a minimum at the equator, consistent with vanishing upper-level zonal wind at $\pm\phi_1$ and easterlies between ϕ_1 and $-\phi_1$.

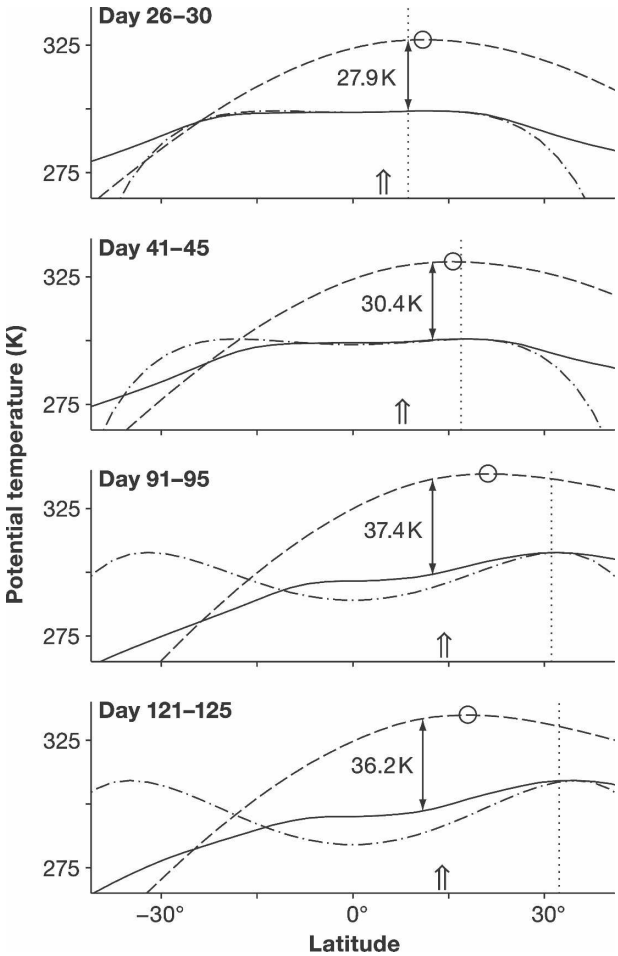

FIG. 8. Mean potential temperature (solid) and corresponding radiative-equilibrium (dashed) and angular momentum–conserving (dashed–dotted) potential temperature at $\sigma = 0.85$ at four pentads. The first three pentads are the same as those for which mean circulations are shown in rows 2–4 of Fig. 5. Circles mark the maximum of the radiative-equilibrium potential temperature. Thin double-headed arrows mark the latitude of maximum difference between the mean potential temperature and the radiative-equilibrium potential temperature in the southern Hadley cell, with the potential temperature difference stated next to the arrows. Double arrows mark the latitude of maximum upward mass flux at $\sigma = 0.85$. Dotted lines mark the boundary between the southern and the northern Hadley cell (zero of streamfunction at $\sigma = 0.85$).

For four pentads around the transition into and in the winter regime of the southern Hadley cell, Fig. 8 shows the potential temperature at $\sigma = 0.85$ along with the corresponding radiative-equilibrium and angular momentum–conserving potential temperature. (The difference in potential temperatures at a lower sigma

[3] For analogous considerations for a vertically averaged temperature and for a lower-level moist entropy, see Lindzen and Hou (1988) and Emanuel (1995).

level, as shown in Fig. 8, and at a corresponding lower-level isobar, as considered in the preceding paragraph, is negligible for what follows.) The angular momentum–conserving potential temperature is the potential temperature (7) with ϕ_1 and θ_{max} chosen to match, for each pentad, the maximum actual potential temperature at $\sigma = 0.85$, and with $\theta_0 = 300$ K and $H = 14$ km (approximately the height difference between the level $\sigma = 0.85$ and the tropopause). At day 26–30 and day 41–45, just before and at the transition of the southern Hadley cell into the winter regime (cf. Figs. 5, 6), gradients of the angular momentum–conserving potential temperature are weak within the Hadley cells, and gradients of the actual potential temperature are weaker still, consistent with Ro < 1 in the upper branches of the cells. Because of the weakness already of the gradients of the angular momentum–conserving potential temperature, the actual and the angular momentum–conserving potential temperature are difficult to distinguish within the Hadley cells, except in the descending branches, although the Hadley cells are far from angular momentum conserving (Fig. 5). At day 91–95 and day 121–125, in the winter regime of the southern Hadley cell, the potential temperature in the summer hemisphere decreases from a subtropical maximum toward the equator. But the potential temperature decrease is slower than that of the corresponding angular momentum–conserving potential temperature (7), although streamlines in the ascending branch of the southern Hadley cell follow angular momentum contours closely (Fig. 5). The potential temperature decreases more slowly toward the equator primarily because the ascending branch of the southern Hadley cell is not concentrated near the latitude of the potential temperature maximum (see Fig. 5 and double arrows in Fig. 8). Most ascent occurs at lower latitudes, in regions not of negligible lower-level zonal winds but of strong westerlies (Figs. 5, 6), and brings air with higher absolute angular momentum into the upper troposphere. In the summer hemisphere, this still leads to upper-level easterlies and poleward gradients of lower-level potential temperatures equatorward of the highest latitude of ascent, albeit weaker easterlies and potential temperature gradients than the idealizations (6) and (7) suggest.[4] In the winter hemisphere, eddy fluxes lead to significant deviations from angular momentum conservation in the free troposphere so that the angular momentum–conserving potential temperature (7) is inadequate even as a qualitative idealization of the lower-level potential temperatures. Nonetheless, upper-level easterlies extend into the winter hemisphere (Fig. 6c), but, unlike in the idealization (6), they are not symmetric about the equator. Similar observations apply to the steady-state simulations in Fig. 3.

At and above the sigma level at which the potential temperatures in Fig. 8 are shown, the Newtonian relaxation time is constant (50 days), so the difference between the actual potential temperature and the radiative-equilibrium potential temperature is proportional to the radiative heating rate (provided one again neglects pressure variations along the sigma level). In the winter regime of a Hadley cell, the difference between these potential temperatures and thus the radiative heating rate at $\sigma = 0.85$ attain their maximum values between 10° and 13° latitude in the summer hemisphere, near the latitude of maximum upward mass flux (see day 91–95 and day 121–125 in Fig. 8).

The maximum radiative heating rate increases at the transition of a Hadley cell from the equinox into the winter regime, in part because the radiative-equilibrium potential temperature increases and in part because the actual potential temperature decreases near the radiative heating maximum. From day 41–45 to day 91–95, at the latitude of maximum radiative heating in the southern Hadley cell (equal to 12.5° in both pentads),[5] the radiative-equilibrium potential temperature increases by 5.9 K, but the actual potential temperature decreases by 1.1 K, resulting in an increase in their difference by 7.0 K (Fig. 8). As the Hadley cell strengthens and poleward lower-level potential temperature gradients increase at the transition, the cross-equatorial advection of relatively cold air at lower levels strengthens, leading to cooling near the radiative heating maximum. The potential temperature maximum and the boundary between the southern and the northern Hadley cell (vertical dotted lines in Fig. 8) shift poleward of the radiative heating maximum and even poleward of the radiative-equilibrium potential temperature maximum (circles in Fig. 8).[6] The pole-

[4] In the summer hemisphere, the assumption in (7) of a latitude-independent tropospheric temperature lapse rate is unproblematic in our simulation because except in the descending branches and at lower levels in the winter hemisphere, where an inversion layer forms, lapse rates in the Hadley cells above the planetary boundary layer are approximately equal to the constant convective lapse rate (see Fig. 11 below).

[5] At day 41–45, maximum potential temperature difference in the southern Hadley cell indicated in Fig. 8 is not a global maximum. A maximum with a slightly greater potential temperature difference (31.0 K) occurs at 33° latitude in the northern Hadley cell. This maximum is transient; it does not occur in the steady-state simulations.

[6] The radiative-equilibrium potential temperature maxima at $\sigma = 0.85$ lie within 2° of ϕ_0.

ward shift in the lower-level potential temperature maximum implies a poleward shift in the boundary between the southern and the northern Hadley cell because the boundary is approximately colocated with the maximum—as it must be, by gradient wind balance, if the ascent near the boundary is nearly vertical and angular momentum conserving so that the vertical zonal-wind shear there approximately vanishes (Privé and Plumb 2007a,b).

To see how the increase in the maximum radiative heating rate and the poleward shift in the boundary between the southern and the northern Hadley cell lead to an increase in strength of the cross-equatorial cell, consider the thermodynamic balance of an atmospheric column,

$$\partial_t\langle\overline{\theta}^{\sigma}\rangle + \mathrm{div}\,\langle\overline{v}^{\sigma}\overline{\theta}^{\sigma} + \overline{v'\theta'}^{\sigma}\rangle = \langle\overline{Q}_r^{\sigma}\rangle + \langle\overline{Q}_o^{\sigma}\rangle. \quad (8)$$

Here θ is potential temperature, Q_r and Q_o are the potential temperature tendencies owing to radiation (Newtonian temperature relaxation) and to other diabatic processes, and $\langle\cdot\rangle = g^{-1}\int \overline{p}_s\,(\cdot)\,d\sigma$ denotes a column integral. Figure 9 shows the column heating rates owing to radiation $c_p\langle\overline{Q}_r^{\sigma}\rangle$, to the mean potential temperature flux convergence $-c_p\mathrm{div}\,\langle\overline{v}^{\sigma}\overline{\theta}^{\sigma}\rangle$, and to the eddy potential temperature flux convergence $-c_p\mathrm{div}\,\langle\overline{v'\theta'}^{\sigma}\rangle$, as well as the residual $c_p\partial_t\langle\overline{\theta}^{\sigma}\rangle - c_p\langle\overline{Q}_o^{\sigma}\rangle$. Diabatic processes contributing to the heating rate $c_p\langle\overline{Q}_o^{\sigma}\rangle$ include the parameterized convection, which conserves enthalpy but not potential temperature integrated over a column, and other subgrid-scale processes. The residual $c_p\partial_t\langle\overline{\theta}^{\sigma}\rangle - c_p\langle\overline{Q}_o^{\sigma}\rangle$ is generally small compared with the other terms in the thermodynamic balance (8).

The mean potential temperature flux $\langle\overline{v}^{\sigma}\overline{\theta}^{\sigma}\rangle_{\phi}$ at latitude ϕ is related to the integral of the divergence from the boundary ϕ_b between the southern and the northern Hadley cell to latitude ϕ by

$$\langle\overline{v}^{\sigma}\overline{\theta}^{\sigma}\rangle_{\phi}\cos\phi = \int_{\phi_b}^{\phi} \mathrm{div}\,\langle\overline{v}^{\sigma}\overline{\theta}^{\sigma}\rangle_{\phi'}\cos\phi'\,d\phi', \quad (9)$$

provided the boundary between the cells is vertical such that the mean meridional mass flux vanishes throughout the column there, as is approximately the case in our simulation (see Fig. 5). So the shaded areas in Fig. 9—the areas under the mean convergence curve between ϕ_b and the latitude in the southern Hadley cell at which the mean convergence changes sign—are approximately (up to a cosine factor) proportional to the extremal mean potential temperature flux in the southern Hadley cell and thus are indicative of the strength of the southern Hadley cell. (Because the potential temperature flux above the tropopause is weak, the distinction between integrals over the entire column and integrals only over the Hadley cell is negligible.) The mean potential temperature flux is related to the mean mass flux via the gross (dry) stability

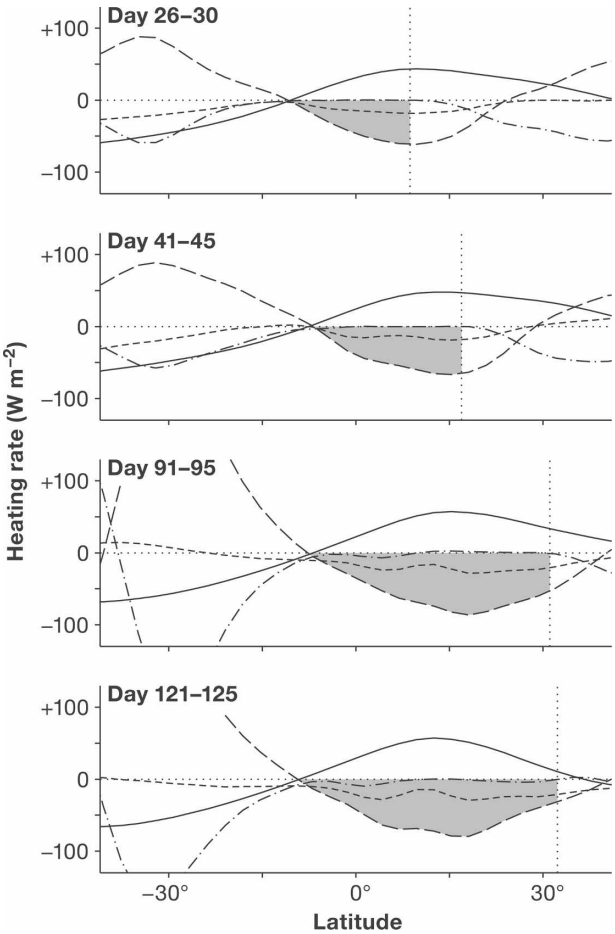

FIG. 9. Mean column heating rates owing to radiation (solid), mean potential temperature flux convergence (long dashed), and eddy potential temperature flux convergence (dashed–dotted), as well as residual (short dashed) at the same four pentads as in Fig. 8. As in Fig. 8, vertical dotted lines mark the boundary between the southern and the northern Hadley cell. The shaded areas are approximately proportional to the extremal mean potential temperature flux in the southern Hadley cell.

$$\Delta_v(\phi) = -\frac{2\pi a\cos\phi\,\langle\overline{v}^{\sigma}\overline{\theta}^{\sigma}\rangle_{\phi}}{\Psi_{\mathrm{ext}}(\phi)}, \quad (10)$$

the effective potential temperature difference between the upper and lower branch of the mean meridional circulation, where $\Psi_{\mathrm{ext}}(\phi)$ is the extremal value of its streamfunction in the column at latitude ϕ (Neelin and Held 1987; Held 2000, 2001; Neelin 2007). Because the gross stability in the Hadley cells varies with latitude, particularly in the cross-equatorial winter cell, the latitudes of the extrema of the mean potential temperature

flux and of the mean mass flux do not necessarily coincide, as is evident by comparison of Figs. 5 and 9. However, despite variations in the gross stability (discussed further in section 6), the extremal mean potential temperature flux and mean mass flux vary similarly over the seasonal cycle. Taking the extremal mean potential temperature flux and thus the shaded areas in Fig. 9 as indicative of the strength of the cross-equatorial Hadley cell is adequate for the qualitative argumentation that follows.

Figures 8 and 9 taken together reveal a feedback responsible for the strengthening of the cross-equatorial Hadley cell at the transition into the winter regime. As the latitude ϕ_0 of maximum radiative-equilibrium temperature moves poleward, so does the boundary between the winter and the summer cell, leading, by angular momentum conservation, to strengthening upper-level easterlies in the summer hemisphere. Because the energy-containing midlatitude eddies cannot penetrate into regions of upper-level easterlies, the eddy potential temperature flux in the summer hemisphere is weak compared with the mean flux so that the radiative heating is primarily balanced by divergence of the mean potential temperature flux (Fig. 9). According to relation (9), provided the column radiative heating rate in the latitude zone of the cross-equatorial Hadley cell increases or does not decrease significantly, the poleward shift of the boundary between the winter and the summer cell leads to an increase in the extremal mean potential temperature flux (shaded areas in Fig. 9) and thus in the mean mass flux in the cross-equatorial Hadley cell. The poleward advection of relatively cold air up the temperature gradient at lower levels in the summer hemisphere strengthens—both because the mean mass flux strengthens and because, by angular momentum conservation, the poleward temperature gradient increases. This pushes the lower-level temperature maximum and, with it, the boundary between the winter and the summer cell and some (though not all) ascent farther poleward, leading to further strengthening of the cross-equatorial Hadley cell. Energy constraints, the increasing poleward temperature gradient demanded by angular momentum conservation, and the requirement that temperatures are continuous at the boundary between the winter and the summer cell ultimately arrest the feedback and limit the poleward movement of the boundary between the cells.

This feedback between nonlinear mean-flow processes acts when the flow in the summer hemisphere is nearly angular momentum conserving, such that a cross-equatorial Hadley cell in the summer hemisphere can respond directly to variations in thermal driving (although eddy fluxes still play a significant role in the winter hemisphere). It underlies the rapid poleward shift of the boundary between the Hadley cells and the strengthening of the cross-equatorial cell as ϕ_0 increases away from zero in the nearly inviscid axisymmetric theory of Lindzen and Hou (1988). The analysis in section 4 implies, however, that arguments predicated on angular momentum conservation in the free troposphere and thus nearly inviscid axisymmetric theories are not applicable throughout the seasonal cycle and not even over the entire extent of the cross-equatorial Hadley cell.

The transitions of a Hadley cell between the regimes and the rapid shift in the latitude of the streamfunction extremum are mediated by another feedback, between eddies and the upper-level zonal winds. As a Hadley cell strengthens at the transition into the winter regime, the upper-level easterlies strengthen not only in the summer hemisphere but increasingly extend into the winter hemisphere (see Fig. 6c and also the steady-state simulations in Fig. 3). In its ascending branch and near its emerging streamfunction extremum near the equator or in the summer hemisphere, the cross-equatorial Hadley cell is increasingly well shielded from midlatitude eddies in the winter hemisphere (cf. Charney 1969; Webster and Holton 1982), allowing it to approach the angular momentum–conserving limit more closely and over a broader latitude band. This in turn leads to strengthening and extension into the winter hemisphere of upper-level easterlies. By this eddy–mean flow feedback, the nonlinear mean-flow processes that strengthen the mean meridional mass flux in the summer hemisphere separate latitudinally from the eddy fluxes in the winter hemisphere that influence the mean meridional mass flux there. The increasing latitudinal separation of the mean meridional mass flux in the summer hemisphere from that associated with eddies in the winter hemisphere is also recognizable in Fig. 4 for the steady-state simulations, which shows that, as $|\phi_0|$ increases, the extremum of the streamfunction component associated with eddy momentum fluxes moves toward the winter pole.

When the mean meridional mass flux associated with nonlinear mean flow processes in the summer hemisphere exceeds the mean meridional mass flux that is, at least partially, associated with eddy fluxes in the winter hemisphere, the global streamfunction extremum transfers from the winter toward or, in our simulation, into the summer hemisphere and thus appears to move rapidly toward or into the summer hemisphere (see the steady-state streamfunction components in Fig. 4). The transfer may occur via a transition state in which separate local streamfunction extrema exist, as at day 41–45 in Fig. 5. For the transfer to occur, it is essential that for

sufficiently large ϕ_0, the mean meridional mass flux as a function of ϕ_0 strengthens more rapidly by nonlinear mean-flow processes in the summer hemisphere than by eddy fluxes in the winter hemisphere. At the regime transition, the different dependences on ϕ_0 manifest themselves in a changed dependence of Hadley cell strength on ϕ_0, as is evident in the steady-state simulations (Fig. 2).

The feedbacks involving nonlinear mean-flow processes and eddy–mean flow interactions at the transitions between the regimes account qualitatively for the rapid shifts in latitude of the streamfunction extremum, for the changes in Hadley cell strength, for the shifts in the dominant zonal momentum balance, and for the changes in direction and strength of the zonal wind both at upper levels (by angular momentum conservation) and at lower levels (by the boundary layer zonal momentum balance). While we have focused on the transition into the winter regime, it is clear that reverse feedback mechanisms act at the transition from the winter into the equinox regime.

6. Dynamics of lower-level convergence zones

The above argumentation alone does not account for the rapidity of the changes in maximum upward mass flux at the regime transitions of the Hadley cells (Fig. 6a), and it does not account for the position of the main lower-level convergence zone in the winter regime (Figs. 3, 5, and 6b). In the winter regime, the lower-level upward mass flux is maximal near the radiative heating maximum (Fig. 8), but the latitude variations of the lower-level and column radiative heating rate (Figs. 8 and 9) are smoother than those of the lower-level upward mass flux. The distribution of the upward mass flux is not determined by the distribution of the radiative heating alone. Considerations of a simplified momentum balance illuminate the dynamics of the lower-level convergence zones.

Representing turbulent drag as Rayleigh drag with damping coefficient ε, we consider the pressure-coordinate mean zonal and meridional momentum equations in the planetary boundary layer in a statistically steady state,

$$-(f+\bar{\zeta})\bar{v} \approx -\varepsilon\bar{u}, \tag{11a}$$

$$(f+\bar{\zeta})\bar{u} \approx -\varepsilon\bar{v} - \partial_y\overline{B}, \tag{11b}$$

where the bar again denotes a temporal and zonal mean along isobars and $\overline{B} = \overline{\Phi} + (\bar{u}^2 + \bar{v}^2)/2$ is the mean barotropic Bernoulli function with geopotential Φ. Neglected in these momentum equations are the divergence of large-scale eddy momentum fluxes and the vertical advection of momentum by the mean meridional circulation, which are much smaller than the retained terms in our simulation. Writing the absolute vorticity again in terms of the local Rossby number, $(f + \bar{\zeta}) = f(1-\mathrm{Ro})$, we can express the zonal and meridional velocity as implicit functions,

$$\bar{u} \approx -\frac{1 - G(\phi, \mathrm{Ro})}{f(1-\mathrm{Ro})}\,\partial_y\overline{B}, \tag{12a}$$

$$\bar{v} \approx -\frac{G(\phi, \mathrm{Ro})}{\varepsilon}\,\partial_y\overline{B}, \tag{12b}$$

where G is the nondimensional function

$$G(\phi, \mathrm{Ro}) = \frac{\varepsilon^2}{\varepsilon^2 + f^2(1-\mathrm{Ro})^2}. \tag{13}$$

The function G takes values between 0 and 1: $G \to 1$ if $f^2(1-\mathrm{Ro})^2 \ll \varepsilon^2$, implying that the term on the left-hand side of the meridional momentum equation (11b) is negligible and the Bernoulli gradient is primarily frictionally balanced; and $G \to \varepsilon^2/[f^2(1-\mathrm{Ro})^2] \to 0$ if $f^2(1-\mathrm{Ro})^2 \gg \varepsilon^2$, implying that the frictional term in the meridional momentum equation (11b) is negligible and the Bernoulli gradient is primarily balanced by the term on the left-hand side. The midpoint value $G(\phi_c, \mathrm{Ro}) = 0.5$, attained at transition latitudes $\phi_c(\mathrm{Ro})$ at which $f^2(1-\mathrm{Ro})^2 = \varepsilon^2$, can be taken as demarcating these two limits. Comparison of the expressions for the zonal and meridional velocity shows that $|\bar{u}| \ll |\bar{v}|$ in the limit $G \to 1$ and $|\bar{u}| \gg |\bar{v}|$ in the limit $G \to 0$. Near the transition latitudes, wind vectors turn from predominantly meridional to predominantly zonal, with $|\bar{u}| \approx |\bar{v}|$ at $\phi_c(\mathrm{Ro})$.

The expressions (12) for the velocities are convenient in analyses of the dynamics of lower-level convergence zones, particularly if the Bernoulli gradient varies on larger scales than the function G. The linear limit ($\mathrm{Ro} \to 0$ and $\partial_y\overline{B} \to \partial_y\overline{\Phi}$) of the boundary layer momentum equations (11) and of the expressions (12) for the velocities has been discussed by several authors in studies of lower-level convergence zones (e.g., Lindzen and Nigam 1987; Pauluis 2004). In the linear limit, the right-hand side of the expressions (12) for the velocities no longer depends explicitly on the velocities. Tomas et al. (1999) considered nonlinear boundary layer momentum equations similar to Eqs. (11) to study how nonlinear momentum advection modifies lower-level convergence zones [see Sobel and Neelin (2006) and Sobel (2007) for an overview of this literature]. We will use the expressions (12) diagnostically to analyze the lower-level dynamics in our simulation.

Figure 10 shows the function G for $\mathrm{Ro} = 0$ and for the latitude-dependent local Rossby number at day 91–95 at the near-surface level $\sigma = 0.95$, which is near the

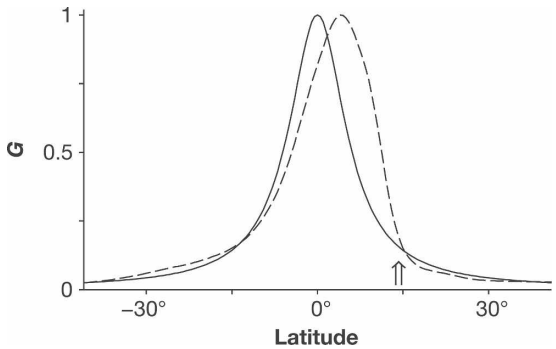

FIG. 10. Function $G(\phi, \mathrm{Ro})$ with $\varepsilon = (0.75\ \mathrm{day})^{-1}$ for Ro = 0 (solid) and for the latitude-dependent local Rossby number at $\sigma = 0.95$ at day 91–95 (dashed). As in Fig. 8, the double arrow marks the latitude of maximum upward mass flux at $\sigma = 0.85$.

core of the lower branch of the cross-equatorial Hadley cell (see Fig. 5). We chose $\varepsilon = (0.75\ \mathrm{day})^{-1}$ in the figure, based on a rough fit of the zonal momentum Eq. (11a) to the simulated velocity fields; however, as we discuss further below, a constant damping coefficient ε is not quantitatively accurate at all latitudes, particularly not on the winter side of the maximum of G. The function G for Ro = 0 decreases monotonically poleward from the maximum value $G = 1$ at the equator, reaching the midpoint value $G = 0.5$ at the transition latitudes at which $f^2 = \varepsilon^2$, or, in the small-angle approximation (cf. Young 1987),

$$\phi_c(0) \approx \pm \frac{\varepsilon}{2\Omega}. \tag{14}$$

With our parameter values, the transition latitudes are $\phi_c(0) \approx \pm 6°$. Nonlinear momentum advection modifies the function G for the latitude-dependent local Rossby number, primarily in that the poleward decrease of G in the summer hemisphere is sharper and the maximum of G and the summer-hemisphere transition latitude $\phi_c(\mathrm{Ro})$ are displaced toward the summer pole. The displacement of the maximum and of the transition latitude toward the summer pole is consistent with Ro > 1 within a few degrees of the equator in the boundary layer in the summer hemisphere, as discussed in section 4, and with an associated displacement toward the summer pole of the latitude at which the boundary layer absolute vorticity vanishes (Ro = 1) and the function G attains its maximum value.[7] In the winter hemisphere poleward of about 10° latitude and in the summer hemisphere poleward of the latitude of maximum upward mass flux (marked by the double arrow in Fig. 10), nonlinear momentum advection modifies the function G only marginally.

The poleward decrease of G around the transition latitude in the summer hemisphere accounts for the position of the main lower-level convergence zone in the winter Hadley cell. Consider first the linear limit with $\mathrm{Ro} \to 0$ and $\partial_y \overline{B} \to \partial_y \overline{\Phi}$. In the winter Hadley cell, consistent with cross-equatorial flow down the geopotential gradient, the geopotential in the boundary layer decreases along isobars from the winter into the summer hemisphere toward a minimum that approximately coincides with the maximum in lower-level temperatures (cf. Fig. 8). To the extent that the relation (12b) for the meridional velocity is adequate and the geopotential gradient varies on larger scales than the function G, the poleward decrease of G around the transition latitude $\phi_c(0)$ in the summer hemisphere implies lower-level convergence $-\mathrm{div}\ \overline{v} > 0$ around the transition latitude. Nonlinear momentum advection, discussed further below, sharpens the poleward decrease of G in the summer hemisphere and displaces the summer hemisphere transition latitude $\phi_c(\mathrm{Ro})$ poleward, which, taken by itself, implies a corresponding sharper localization and poleward displacement of the lower-level convergence zone. Figure 10 shows that the lower-level upward mass flux indeed is maximal near the transition latitude, where the poleward decrease of G is sharpest. Tomas et al. (1999) suggested that lower-level convergence in a cross-equatorial Hadley cell is located poleward of the latitude at which the absolute vorticity vanishes. Our analysis suggests that the transition latitudes $\phi_c(\mathrm{Ro})$ at which $(f + \overline{\zeta})^2 = \varepsilon^2$ and G decreases sharply characterize the position of the convergence zones more precisely. Because nonlinear modifications of G poleward of this main lower-level convergence zone are small and the Bernoulli gradient is dominated by the geopotential gradient in the vicinity of the convergence zone, the poleward decrease of G in the convergence zone marks a transition in the dominant balance of the meridional geopotential gradient in the boundary layer from nonlinear-frictional to geostrophic. See Waliser and Somerville (1994) for similar considerations for the linear limit.

The poleward decrease of G around the transition latitude in the summer hemisphere also accounts for the rapidity of the changes in maximum upward mass flux at the regime transitions of the Hadley cells. At the transition of a Hadley cell from the equinox into the winter regime, the boundary between the winter and the summer cell shifts toward the summer pole, such

[7] The condition Ro > 1 is a necessary condition for inviscid inertial instability; however, because of turbulent drag and the finite vertical extent of the boundary layer, Ro > 1 in the boundary layer does not necessarily imply that inertial instability does in fact occur (Tomas et al. 1999).

that the cross-equatorial meridional mass flux in the boundary layer in the summer hemisphere extends to the Ro = 0 transition latitude $\phi_c(0)$ and beyond. Immediately before the cross-equatorial mass flux in the summer hemisphere extends to the transition latitude $\phi_c(0)$, the transition latitude lies in the summer Hadley cell with weak equatorward mass flux in the boundary layer. When the poleward mass flux in the boundary layer in the summer hemisphere first extends beyond the transition latitude $\phi_c(0)$, a convergence zone forms around $\phi_c(0)$. This convergence zone then is modified by nonlinear advection of momentum from the winter hemisphere and from lower latitudes in the summer hemisphere toward the convergence zone (Fig. 6d). Consistent with the expression (12a) for the zonal velocity, this leads to lower-level westerlies with anticyclonic shear equatorward of the convergence zone (Figs. 5 and 6d), and hence to Ro > 0 and to a poleward displacement of the transition latitude and a sharpening of the poleward decrease of G. Because the localization of the poleward decrease of G leads to localization of the upward mass flux, the maximum upward mass flux increases rapidly as the boundary between the winter and the summer cell shifts toward the summer pole and the meridional mass flux in the boundary layer strengthens. A reverse succession of processes accounts for the rapid decrease in maximum upward mass flux at the transition of a Hadley cell from the winter into the equinox regime.

The poleward decrease of G in the summer hemisphere thus accounts for some aspects of the dynamics of the main lower-level convergence zone. However, inferring characteristics of the convergence zone from the structure of G alone is problematic and not completely satisfactory for three reasons. First, variations of the geopotential gradient and of the Bernoulli gradient are not negligible and contribute to the localization of the lower-level convergence zone near the transition latitude. In a more complete account of the lower-level dynamics, their variations should be coupled to those of the near-surface and interior-atmosphere flow. Second, if the relative vorticity term $\overline{u}\overline{\zeta}$ on the left-hand side of the meridional momentum equation (11b) is taken into account, so should the kinetic energy term $\partial_y\, \overline{u}^2/2$ in the Bernoulli gradient. Because there is partial cancellation between the two terms (their sum is the metric term $\overline{u}^2 \tan\phi/a$), nonlinear modifications of the convergence zone are weaker than one might infer from the nonlinear modifications of G alone. Third, the representation of turbulent drag as Rayleigh drag is an oversimplification, at least for our simulation. The boundary layer divergence implied by relation (12b) given the northward increase of G in Fig. 10 on the winter side of its maximum and given the Bernoulli or geopotential gradient from the simulation is an order of magnitude stronger than the actual divergence in the simulation, which is recognizable as the downward mass flux equatorward of the streamfunction extremum of the cross-equatorial Hadley cell in Figs. 5 and 6b. The absence of strong boundary layer divergence on the winter side of the maximum of G is primarily associated with nonlinearities and explicit shear dependence of the turbulent stress, which lead to variations in the effective damping coefficient ε and reduce the divergence (cf. Stevens et al. 2002). The simplified momentum equations (11) therefore only qualitatively account for the dynamics of the lower-level convergence zones.

While the main lower-level convergence zone in the cross-equatorial winter Hadley cell is relatively sharply localized, the latitude variations of the column radiative heating rate in the vicinity of the convergence zone are smooth because the angular momentum–conserving potential temperature (7) varies smoothly and the radiative heating is a smooth function of temperature (or potential temperature) in our GCM. Because the column radiative heating rate in the summer hemisphere is primarily balanced by the mean potential temperature flux divergence, the mean potential temperature flux divergence in the summer hemisphere likewise varies smoothly with latitude (Fig. 9). The relatively sharper variations in the lower-level mean mass flux divergence must therefore be associated with variations in gross stability (10). The lower-level mean mass flux decreases poleward across the main convergence zone, so gross stabilities must increase poleward across the convergence zone. This is indeed the case in our simulation. It manifests itself in that a significant part of the upper branch of the mean meridional circulation is relatively shallow equatorward of the main lower-level convergence zone, whereas it is deeper poleward thereof (see Fig. 5, day 91–95; or Fig. 3, $\phi_0 = 16°$). Because the thermal stratification in the summer hemisphere is nearly uniform, with a temperature lapse rate approximately equal to the convective lapse rate (Fig. 11), this results in smaller gross stabilities equatorward of the convergence zone than poleward thereof. A similar adjustment of the circulation and gross stability must occur whenever the net heating of an atmospheric column varies on larger scales than the upward mass flux (Held 2000); it is not specific to the radiative-heating formulation in our GCM.

7. Implications for monsoon dynamics

As discussed in the introduction, the local Rossby number in the upper branches of Earth's Hadley cells

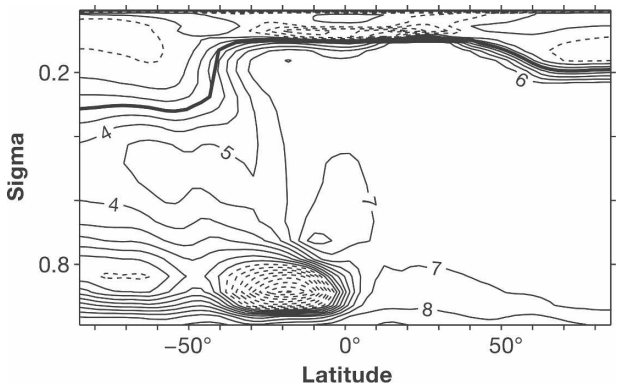

FIG. 11. Mean temperature lapse rate at day 91–95 (contour interval 1 K km^{-1}, negative contours dashed). The thick line marks the tropopause, determined columnwise as an upper level at which the lapse rate is equal to 2 K km^{-1}. The convective lapse rate is 6.8 K km^{-1}.

varies between Ro $\lesssim$ 0.2 in the summer cell and Ro $\gtrsim$ 0.5 in the cross-equatorial winter cell, with Ro $\approx$ 0.7 in the Asian summer monsoon anticyclone. In the course of the seasonal cycle, then, the influence of eddy momentum fluxes on the strength of Earth's Hadley cells varies between strong and at least regionally weak, with the seasonal cycle of the relevant nondimensional influence measure—the local Rossby number—resembling that in our simulation.[8] The implication is that the large-scale dynamics and feedbacks exposed in our idealized simulation are relevant for Earth's atmosphere, particularly for large-scale monsoon regions where the summer mean meridional circulation approaches the angular momentum–conserving limit most closely.

The transitions of the simulated Hadley cells from the equinox into the winter regime and vice versa indeed resemble the onset and end of large-scale monsoons, particularly of the Asian summer monsoon. For example, at the onset of the Asian summer monsoon

(i) lower-level westerlies and upper-level easterlies develop (e.g., Yin 1949; Webster 1987), as at the transitions in the simulation (Figs. 6c,d and 7b);
(ii) tropospheric temperature gradients reverse, with temperatures increasing poleward south of the Tibetan Plateau (e.g., Li and Yanai 1996), as at the transitions in the simulation (Fig. 8);
(iii) the intertropical convergence zone shifts rapidly from an equatorial position to a subtropical monsoonal position (e.g., Lau and Yang 1996), similarly to the lower-level convergence zone at the transitions in the simulation (Figs. 5 and 6b), although the latitude shifts in the simulation are not as large as those observed, for example, over India.

Moreover, the near-surface meridional velocity near the equator reaches about 7 m s^{-1} in the cross-equatorial Hadley cell in our simulation and reverses seasonally, similarly to the meridional flow in the Earth's large-scale monsoon regions. Our simulation exhibits all features traditionally viewed as characteristic of monsoons, whether one takes the reversal of lower-level winds or the shift in the lower-level convergence zone as defining monsoon transitions (cf. Chao and Chen 2001; Chou et al. 2001; Gadgil 2003)—all features except those involving precipitation, which was not taken into account in the simulation. However, if one takes the lower-level upward mass flux in the simulation as a proxy of precipitation, this too exhibits features characteristic of monsoon transitions, such as the rapid local changes at the transitions (Fig. 7a).

Observations (i) and (ii) imply that the feedbacks involving eddy–mean flow interactions and nonlinear mean flow processes discussed in section 5 can act at the onset and end of the Asian summer monsoon, albeit only regionally, not in the statistically axisymmetric form in which we have discussed them. Because the local zonal flow determines the propagation characteristics of the energy-containing midlatitude eddies (Webster and Holton 1982), the eddy–mean flow feedback can act regionally. The feedback between nonlinear mean flow processes can likewise affect the local mean meridional circulation. We therefore conjecture that similar dynamic mechanisms as at the regime transitions in the simulation, acting regionally and modified by inhomogeneities in lower boundary conditions, are implicated in the dynamics of large-scale monsoon transitions in Earth's atmosphere.[9] Because these dynamic mechanisms can act irrespective of land–sea contrasts and other inhomogeneities in lower boundary conditions, this conjecture, if correct, would imply that the principal role of an off-equatorial landmass in monsoon transitions is to provide a surface of sufficiently low thermal inertia for the feedbacks discussed in section 5 to be able to act on intraseasonal time scales. Low thermal inertia of the surface is necessary for the relatively rapid poleward shift of the near-surface tem-

[8] Even in a local rather than a zonal mean, when the mean zonal momentum equation contains zonal advection terms not included in Eq. (1), the local Rossby number remains a measure of the degree to which the mean meridional flow approaches the angular momentum–conserving limit.

[9] The North American monsoon and possibly other smaller-scale monsoon systems are governed by different dynamics; see Bordoni et al. (2004) and Bordoni and Stevens (2006).

perature maximum and boundary between the winter and the summer Hadley cell and for the relatively rapid establishment of poleward gradients in near-surface temperature in balance with upper-level easterlies. Monsoon transitions would represent regional transitions of the mean meridional circulation between regimes distinguishable according to whether large-scale eddy momentum fluxes strongly or weakly influence the strength of the circulation. While these regime transitions can occur in the absence of inhomogeneities in lower boundary conditions, it remains to be investigated whether such inhomogeneities play an essential or an important but merely modifying role in the monsoon transitions in Earth's atmosphere. The simulations by Chao and Chen (2001) suggest that land–sea contrast may not be essential for the Asian summer monsoon; however, because they used, in place of landmasses, a prescribed seasonally varying sea surface temperature that retained some meridional temperature contrasts, monsoon transitions in their simulations, unlike in our simulation, cannot be viewed as generated solely by internal atmospheric dynamics.

Moisture and an active hydrologic cycle will modify the dynamic mechanisms that we discussed. Limits to the supply of moist static energy and interactions of the large-scale circulation with the gross moist stability can modify the position of lower-level convergence zones (Chou et al. 2001; Chou and Neelin 2003; Privé and Plumb 2007b; Neelin 2007), and additional feedbacks, such as wind-induced surface heat exchange (Neelin et al. 1987; Emanuel 1987; Yano and Emanuel 1991; Numaguti 1995; Yano and McBride 1998), can modify the feedbacks discussed here. However, the regime transitions of the Hadley cells are transitions in the dominant zonal momentum balance, which is not directly affected by moist processes. We have carried out simulations with an idealized GCM that includes a representation of an active hydrologic cycle and a surface of low thermal inertia (Bordoni 2007). Similar regime transitions occur in those simulations, with the difference that lower-level convergence is less strongly controlled by the boundary layer momentum balance and the main convergence and precipitation zone is located farther poleward, near the surface temperature maximum, in closer agreement with observation (iii) for the Asian summer monsoon. We will report these results elsewhere.

8. Open questions

Our discussion of the dynamics of the regime transitions and of the lower-level convergence zones was qualitative. Several quantitative questions have remained unanswered:

(i) When do the regime transitions of a Hadley cell occur? Within our GCM, this is the question at which latitude ϕ_0 the regime transitions occur. More generally, given thermal and radiative properties of the surface and atmosphere, it is the question at which solar declination angle the regime transitions occur.

(ii) How do the meridional extent and strength of a Hadley cell in either regime depend on external factors such as the strength and hemispheric asymmetry of the differential solar heating?

(iii) How do the strength and position of lower-level convergence zones depend on external factors and the large-scale circulation? What is the quantitative role of nonlinear momentum advection and of nonlinearities and explicit shear dependence of the turbulent stress in the boundary layer in controlling the strength and position of the convergence zones?

(iv) What determines the gross stability (vertical structure of meridional mass flux) in a Hadley cell and its variation with latitude?

Because of the central roles of eddy fluxes in the summer and equinox regime of a Hadley cell and of feedbacks between eddies and the mean flow at the regime transitions, questions (i) and (ii) cannot be answered by theories of axisymmetric circulations. For example, the regime transitions that we described differ from the transitions of axisymmetric circulations between a linear viscous regime and a nonlinear, nearly angular momentum–conserving regime described by Plumb and Hou (1992). The axisymmetric transitions occur in response to variations in thermal driving that is localized off the equator. As discussed by Plumb and Hou, they do not occur if, as is the case in our simulations, radiative-equilibrium temperatures have a nonzero meridional gradient at the equator. And nearly inviscid axisymmetric theories such as that of Lindzen and Hou (1988) may illuminate some aspects of the winter regime of a Hadley cell, but they do not account for the seasonal variations in meridional extent and strength of a Hadley cell (Walker and Schneider 2005).

To answer questions (i) and (ii), we need a theory of Hadley cells that couples a nonlinear mean meridional circulation to eddy fluxes, which depend on circulation statistics determined by the mean meridional circulation, eddy fluxes, and radiative and convective processes (cf. Walker and Schneider 2006). Extending the shallow-water or two-layer models commonly used in studies of axisymmetric Hadley circulation dynamics by including a representation of eddy fluxes that depends on the mean circulation state may be a starting point.

Questions (iii) and (iv) are related in that the posi-

tion and strength of lower-level convergence zones and the gross stability are related and may be mutually dependent on each other. Because the gross stability links the mass and thermodynamic balances of a Hadley cell, how it is determined also affects the question of how the strength of a Hadley cell depends on external factors.

These questions need to be resolved for a more complete understanding even of the statistically axisymmetric dry dynamics that we have discussed. Additional questions arise when there are inhomogeneities in lower boundary conditions and when moist processes are active and affect particularly the gross moist stability of the circulation. For example, the question of what determines the strength and position of precipitation zones arises, given that precipitation zones are not necessarily colocated with lower-level convergence zones, which can be associated with relatively shallow nonprecipitating circulations (e.g., Zhang et al. 2004; Sobel and Neelin 2006; Sobel 2007).

9. Conclusions

We have shown that, in the course of a simulated seasonal cycle, Hadley cells undergo transitions between regimes distinguishable according to whether eddy momentum fluxes strongly or weakly influence the strength of the cells. The dominant zonal momentum balance at the center of a Hadley cell shifts at the transitions between the regimes, from eddies dominating the momentum flux divergence in the summer and equinox cell to the mean meridional circulation dominating in the winter cell. At the transitions, the latitude of the streamfunction extremum shifts rapidly, the Hadley cell strength and maximum upward mass flux change, and the direction and strength of the zonal wind at upper and lower levels change. A feedback between nonlinear mean-flow processes leads to the changes in strength of a Hadley cell at the regime transitions, and an eddy–mean flow feedback mediates the transitions and the rapid shifts in the latitude of the streamfunction extremum. Considerations of the momentum balance in the planetary boundary layer show that the maximum upward mass flux occurs in an off-equatorial convergence zone located where the balance of the meridional geopotential gradient in the planetary boundary layer shifts from nonlinear–frictional to geostrophic.

As in our simulation, the influence of eddy momentum fluxes on the strength of Earth's Hadley cells varies between strong (summer cell) and weak (winter cell in large-scale monsoon regions). This indicates that the large-scale dynamics and feedbacks exposed in our idealized simulation are relevant for Earth's atmosphere, particularly for large-scale monsoon regions. The regime transitions in our simulation resemble the onset and end of monsoons, and we conjecture that similar dynamic mechanisms as in the simulation, acting regionally, are implicated in the dynamics of the large-scale monsoon circulations in Earth's atmosphere. This would imply that the fundamental dynamic mechanisms involved in monsoon transitions are independent of inhomogeneities in lower boundary conditions. The principal role of an off-equatorial landmass would be to provide a surface of sufficiently low thermal inertia for the mean flow and eddy–mean flow feedbacks to be able to act on intraseasonal time scales; inhomogeneities in thermal inertia would not be essential. This view accords a central role to eddies of midlatitude origin in monsoon transitions. Their dependence on the tropical mean meridional circulation and on midlatitude mean flow quantities needs to be understood for a quantitative account of the transitions.

Acknowledgments. We are grateful for support by the National Science Foundation (Grant ATM-0450059), by the National Aeronautics and Space Administration (Grant NAG512559), by a David and Lucile Packard Fellowship, and by a UCLA Dissertation Year Fellowship. We thank Chris Walker for assistance with the GCM and related software and Paul O'Gorman, Bjorn Stevens, and Duane Waliser for helpful comments on drafts of this paper. The simulations reported in this paper were carried out on Caltech's Geological and Planetary Sciences Dell cluster.

REFERENCES

Bordoni, S., 2007: On the role of eddies in monsoonal circulations: Observations and theory. Ph.D. thesis, University of California, Los Angeles, 223 pp.

——, and B. Stevens, 2006: Principal component analysis of the summertime winds over the Gulf of California: A gulf surge index. *Mon. Wea. Rev.,* **134,** 3395–3414.

——, P. E. Ciesielski, R. H. Johnson, B. D. McNoldy, and B. Stevens, 2004: The low-level circulation of the North American monsoon as revealed by QuikSCAT. *Geophys. Res. Lett.,* **31,** L10109, doi:10.1029/2004GL020009.

Chao, W. C., and B. Chen, 2001: The origin of monsoons. *J. Atmos. Sci.,* **58,** 3497–3507.

Charney, J. G., 1969: A further note on large-scale motions in the Tropics. *J. Atmos. Sci.,* **26,** 182–185.

Chou, C., and J. D. Neelin, 2003: Mechanisms limiting the northward extent of the northern summer monsoons over North America, Asia, and Africa. *J. Climate,* **16,** 406–425.

——, ——, and H. Su, 2001: Ocean-atmosphere-land feedbacks in an idealized monsoon. *Quart. J. Roy. Meteor. Soc.,* **127,** 1869–1892.

Emanuel, K. A., 1987: An air–sea interaction model of intraseasonal oscillations in the Tropics. *J. Atmos. Sci.,* **44,** 2324–2340.

——, 1995: On thermally direct circulations in moist atmospheres. *J. Atmos. Sci.,* **52,** 1529–1534.

Gadgil, S., 2003: The Indian monsoon and its variability. *Annu. Rev. Earth Planet. Sci.,* **31,** 429–467.

Held, I. M., 2000: The general circulation of the atmosphere. *Proc. Program in Geophysical Fluid Dynamics,* Woods Hole, MA, Woods Hole Oceanographic Institution. [Available online at hdl.handle.net/1912/15.]

——, 2001: The partitioning of the poleward energy transport between the tropical ocean and atmosphere. *J. Atmos. Sci.,* **58,** 943–948.

——, and A. Y. Hou, 1980: Nonlinear axially symmetric circulations in a nearly inviscid atmosphere. *J. Atmos. Sci.,* **37,** 515–533.

——, and M. J. Suarez, 1994: A proposal for the intercomparison of the dynamical cores of atmospheric general circulation models. *Bull. Amer. Meteor. Soc.,* **75,** 1825–1830.

Hsu, C. J., and R. A. Plumb, 2000: Nonaxisymmetric thermally driven circulations and upper-tropospheric monsoon dynamics. *J. Atmos. Sci.,* **57,** 1255–1276.

Krishnamurti, T. N., P. Ardanuy, Y. Ramanathan, and R. Pasch, 1981: On the onset vortex of the summer monsoons. *Mon. Wea. Rev.,* **109,** 344–363.

Lau, K.-M., and S. Yang, 1996: Seasonal variation, abrupt transition, and intraseasonal variability associated with the Asian summer monsoon in the GLA GCM. *J. Climate,* **9,** 965–985.

Li, C., and M. Yanai, 1996: The onset and interannual variability of the Asian summer monsoon in relation to land–sea thermal contrast. *J. Climate,* **9,** 358–375.

Lindzen, R. S., and S. Nigam, 1987: On the role of sea surface temperature gradients in forcing low-level winds and convergence in the Tropics. *J. Atmos. Sci.,* **44,** 2418–2436.

——, and A. Y. Hou, 1988: Hadley circulations for zonally averaged heating centered off the equator. *J. Atmos. Sci.,* **45,** 2416–2427.

Mapes, B. E., P. Liu, and N. Buenning, 2005: Indian monsoon onset and the Americas midsummer drought: Out-of-equilibrium responses to smooth seasonal forcing. *J. Climate,* **18,** 1109–1115.

Neelin, J. D., 2007: Moist dynamics of tropical convection zones in monsoons, teleconnections, and global warming. *The Global Circulation of the Atmosphere,* T. Schneider and A. H. Sobel, Eds., Princeton University Press, 267–301.

——, and I. M. Held, 1987: Modeling tropical convergence based on the moist static energy budget. *Mon. Wea. Rev.,* **115,** 3–12.

——, ——, and K. H. Cook, 1987: Evaporation–wind feedback and low-frequency variability in the tropical atmosphere. *J. Atmos. Sci.,* **44,** 2341–2348.

Numaguti, A., 1995: Dynamics and energy balance of the Hadley circulation and the tropical precipitation zones. Part II: Sensitivity to meridional SST distribution. *J. Atmos. Sci.,* **52,** 1128–1141.

Pauluis, O., 2004: Boundary layer dynamics and cross-equatorial Hadley circulation. *J. Atmos. Sci.,* **61,** 1161–1173.

Plumb, R. A., 2007: Dynamical constraints on monsoon circulations. *The Global Circulation of the Atmosphere,* T. Schneider and A. H. Sobel, Eds., Princeton University Press, 252–266.

——, and A. Y. Hou, 1992: The response of a zonally symmetric atmosphere to subtropical thermal forcing: Threshold behavior. *J. Atmos. Sci.,* **49,** 1790–1799.

Privé, N. C., and R. A. Plumb, 2007a: Monsoon dynamics with interactive forcing. Part I: Axisymmetric studies. *J. Atmos. Sci.,* **64,** 1417–1430.

——, and ——, 2007b: Monsoon dynamics with interactive forcing. Part II: Impact of eddies and asymmetric geometries. *J. Atmos. Sci.,* **64,** 1431–1442.

Schneider, E. K., 1977: Axially symmetric steady-state models of the basic state for instability and climate studies. Part II: Nonlinear calculations. *J. Atmos. Sci.,* **34,** 280–296.

Schneider, T., 2004: The tropopause and the thermal stratification in the extratropics of a dry atmosphere. *J. Atmos. Sci.,* **61,** 1317–1340.

——, 2006: The general circulation of the atmosphere. *Annu. Rev. Earth Planet. Sci.,* **34,** 655–688.

——, and C. C. Walker, 2006: Self-organization of atmospheric macroturbulence into critical states of weak nonlinear eddy–eddy interactions. *J. Atmos. Sci.,* **63,** 1569–1586.

Smagorinsky, J., S. Manabe, and J. L. Holloway Jr., 1965: Numerical results from a nine-level general circulation model of the atmosphere. *Mon. Wea. Rev.,* **93,** 727–768.

Sobel, A. H., 2007: Simple models of ensemble-averaged tropical precipitation and surface wind, given the sea surface temperature. *The Global Circulation of the Atmosphere,* T. Schneider and A. H. Sobel, Eds., Princeton University Press, 219–251.

——, and J. D. Neelin, 2006: The boundary layer contribution to intertropical convergence zones in the quasi-equilibrium tropical circulation model framework. *Theor. Comput. Fluid Dyn.,* **20,** 323–350.

Stevens, B., J. Duan, J. C. McWilliams, M. Münnich, and J. D. Neelin, 2002: Entrainment, Rayleigh friction, and boundary layer winds over the tropical Pacific. *J. Climate,* **15,** 30–44.

Tomas, R. A., J. R. Holton, and P. J. Webster, 1999: The influence of cross-equatorial pressure gradients on the location of near-equatorial convection. *Quart. J. Roy. Meteor. Soc.,* **125,** 1107–1127.

Uppala, S. M., and Coauthors, 2005: The ERA-40 reanalysis. *Quart. J. Roy. Meteor. Soc.,* **131,** 2961–3012.

Waliser, D. E., and R. C. J. Somerville, 1994: Preferred latitudes of the intertropical convergence zone. *J. Atmos. Sci.,* **51,** 1619–1639.

Walker, C. C., and T. Schneider, 2005: Response of idealized Hadley circulations to seasonally varying heating. *Geophys. Res. Lett.,* **32,** L06813, doi:10.1029/2004GL022304.

——, and ——, 2006: Eddy influences on Hadley circulations: Simulations with an idealized GCM. *J. Atmos. Sci.,* **63,** 3333–3350.

Webster, P. J., 1987: The elementary monsoon. *Monsoons,* J. S. Fein and P. L. Stephens, Eds., John Wiley & Sons, 3–32.

——, and J. R. Holton, 1982: Cross-equatorial response to middle-latitude forcing in a zonally varying basic state. *J. Atmos. Sci.,* **39,** 722–733.

Yang, D.-S., and T. N. Krishnamurti, 1981: Potential vorticity of monsoonal low-level flows. *J. Atmos. Sci.,* **38,** 2676–2695.

Yano, J.-I., and K. A. Emanuel, 1991: An improved model of the equatorial troposphere and its coupling with the stratosphere. *J. Atmos. Sci.,* **48,** 377–389.

——, and J. L. McBride, 1998: An aquaplanet monsoon. *J. Atmos. Sci.,* **55,** 1373–1399.

Yin, M. T., 1949: Synoptic-aerologic study of the onset of the summer monsoon over India and Burma. *J. Meteor.,* **6,** 393–400.

Young, J. A., 1987: Boundary layer dynamics of tropical and monsoonal flows. *Monsoon Meteorology, Monogr. Geol. Geophys.,* Vol. 7, Oxford University Press, 461–500.

Zhang, C., M. McGauley, and N. A. Bond, 2004: Shallow meridional circulation in the tropical eastern Pacific. *J. Climate,* **17,** 133–139.